Radar-Tomographic Bidirectional Method for Quantitative Microwave Breast Imaging

Mutsuki Nakajima and Shouhei Kidera, *Senior Member, IEEE,*

***Abstract*—A bidirectional processing method using radar and tomography approaches is proposed to achieve an accurate dielectric profile reconstruction for breast-cancer microwave imaging. We introduce a tomography-enhanced radar approach to obtain accurate radar profiles for highly heterogeneous media, where the Green's function and clutter components, such as skin reflection, are effectively reconstructed using a contrast source inversion (CSI)-based tomography scheme, *i.e.*, tomography $\rightarrow$ radar " process. Furthermore, this method introduces a radar-enhanced CSI approach to provide accurate dielectric profiles using an appropriate initial estimate through an accuracy-enhanced radar image. The aforementioned bidirectional processing between radar and tomography consequentially upgrades the reconstruction performance of quantitative imaging (*i.e.*, complex permittivity profile reconstruction) for breast media, (radar $\rightarrow$ tomography process). which would improve the recognition rate for cancerous tissues. The Finite-Difference Time-Domain (FDTD) based numerical test, using realistic breast phantoms, demonstrated that the proposed approach considerably enhances the reconstruction accuracy in permittivity and conductivity.**

***Key words*—Microwave ultra wide-band(UWB) breast cancer detection, Radar imaging, Complex permittivity reconstruction, Inverse scattering analysis, Contrast source inversion (CSI).**

I. Introduction

Microwave breast cancer imaging achieves safe, low-cost, compact, pain-free, and frequent (once every few months) monitoring modality, which is hardly accomplished by the existing X-ray mammography technologies. Thus, the microwave-based diagnoses strongly help to increase the currently low cancer examination rate or increase the recognition rate for early-stage cancer at a size of 10 mm [1], [2], which enhances the survival rate through early treatment. Several studies have reported that a distinct dielectric contrast exists between adipose and malignant tumor tissues [3], [4], which contributes to a strong backscattering and leads to a high-contrast images using a focusing algorithm, namely, the radar approach. The radar approach is often called confocal imaging (CI) or beamformer, which coherently synthesizes backscattering signals to enhance spatial resolution [5]–[7]. Although the radar approach has advantages such as low complexity, it cannot retrieve the dielectric property of each tissue. In addition, most radar approaches assume homogeneity for breast media. Thus, they considerably suffer from inaccuracy in the case of highly heterogeneous media, namely dense breasts, because densely distributed glandular tissue generates significant reflection, which elicits a strong response in radar images and false positive diagnoses. A few studies have attempted to modify the propagation model to suit heterogeneous media [8], [9]. Our previous study [9] accurately generated a Green's function for heterogeneous media using the optimizing output obtained by the contrast source inversion (CSI) [10]. This approach also generates a clutter signal using the CSI outputs and can remarkably enhance the signal-to-clutter ratio (SCR). However, certain challenges must be resolved, such as incomplete prior knowledge of dielectric profiles for background media.

Regarding dielectric profile reconstruction, namely quantitative imaging for complex permittivity, there are many studies on inverse scattering (IS) analyses, [11]–[13], particularly the so-called tomography approach, which directly optimizes the spatial profile of complex permittivity by solving the domain integral equation (DIE). However, the aforementioned inverse problem is usually an ill-posed condition and nonlinear problem, which hinges on an accurate reconstruction with a low-complexity algorithm. To alleviate these IS difficulties, many algorithms can be used, such as linear or nonlinear optimizers [12]–[14]. This study focused on the effective IS approach as CSI, which offers a distinct advantage in that it does not require an iterative calculation of the forward solver, such as Finite-Difference Time-Domain (FDTD). Notably, CSI does not only optimize an object function (dielectric profile) but also total electric fields within the entire area of the region of interest (ROI), by minimizing the cost functions defined by the state and data equations. Additionally, this approach has been massively introduced in biomedical applications, such as breast cancer detection [15], [16] or brain cerebral hemorrhage [17], [18]. However, CSI still suffers from inaccuracy in the reconstruction of highly heterogeneous (high contrast) media owing to strong nonlinearity or local optimization issues. To address the above difficulty, certain studies integrating the radar approach have been developed [19]–[21], by narrowing the ROI corresponding to the high-contrast area, *e.g.*, fibroglandular or tumor tissues. Nonetheless, its reconstruction accuracy naturally depends on that of a radar image, which almost always assumes a homogeneous background media. The literature [22] also introduced the time of arrival (TOA) based ROI estimates with average dielectric properties. However, they presume several unpractical assumptions, including one

This research was supported by MEXT/JSPS KAKENHI Grant Number JP20H02161, Japan.

M. Nakajima and S. Kidera are with the Graduate School of Informatics and Engineering, The University of Electro-Communications, Tokyo, 182-8585, Japan. E-mail: kidera@uec.ac.jp HTML: www.ems.cei.uec.ac.jp/index-e.html

where the TOA values from skin, adipose or glandular areas are completely separated, and that these TOAs are converted to the dielectric constant for each area, using geometrical optics approximation. Note that, the study in [23] used prior ultrasound images. However, it required an accurate registration procedure between tomography and ultrasound images.

This paper introduces a bidirectional processing algorithm between the radar and tomography methods. The first processing is "tomography $\rightarrow$ radar," *i.e.*, the CSI-based tomography generates an accurate Green's function with a breast model constituting only skin and adipose tissues, which enhances the reconstruction accuracy of the radar image, provided that it only focuses on a high-contrast area, such as fibroglandular or cancerous tissues. This has been partially investigated previously [9]. In the second process, *i.e.*, "radar $\rightarrow$ tomography", the obtained radar image provides an appropriate initial estimate of the CSI reconstruction by converting the strength of the radar image to the complex permittivity. There are some investigations of dependency of initial guess of the inverse scattering analysis [13]. Several approaches based on the level set algorithm, which defines the boundary of the low and high contrast area to reduce the number of unknowns, have been also developed [24]–[26], using a prior knowledge of dielectric parameter of each tissue. However, there are much few studies to provide a radar image based initial guess for the post IS approach. Thus, the main contributions of this study are as follows:

1) The CSI-based tomography provides an accurate estimation of the Green's function in heterogeneous media and the clutter signal, such as skin surface reflection ("tomography $\rightarrow$ radar" processing).
2) The radar image offers a promising initial estimate for post-CSI quantitative reconstruction ("radar $\rightarrow$ tomography"), and the reconstruction accuracy including the high-contrast area (fibroglandular or tumor tissues) is significantly improved.

The FDTD numerical analysis, using a magnetic resonance imaging (MRI)-derived realistic phantom, showed that the proposed scheme could achieve an accurate dielectric profile reconstruction, thereby increasing the cancer recognition rate.

II. Method

A. Observation Model

Figure 1 shows the 2-dimensional (2-D) configuration of the observation and target models. The array with numerous transmitters and receivers was located within the breast surrounding area, denoted by $\Omega_{\rm S}$. The inner area of the breast was defined as the ROI, denoted by $\Omega_{\rm D}$, and the breast comprised skin, adipose, fibroglandular, and tumor tissues, each of which exhibited dispersive and isotropic dielectric properties. $E^{\rm T}(\omega;\boldsymbol{r}_{\rm T},\boldsymbol{r}_{\rm R})$ and $E^{\rm I}(\omega;\boldsymbol{r}_{\rm T},\boldsymbol{r}_{\rm R})$ represent the observed total electric fields with and without the breast media, respectively, which are illuminated by the point-source transmitter located at $\boldsymbol{r}_{\rm T}$ and received at $\boldsymbol{r}_{\rm R}$. $E^{\rm S}(\omega;\boldsymbol{r}_{\rm T},\boldsymbol{r}_{\rm R}) \equiv E^{\rm T}(\omega;\boldsymbol{r}_{\rm T},\boldsymbol{r}_{\rm R}) - E^{\rm I}(\omega;\boldsymbol{r}_{\rm T},\boldsymbol{r}_{\rm R})$ is also defined as a scattering electric field.

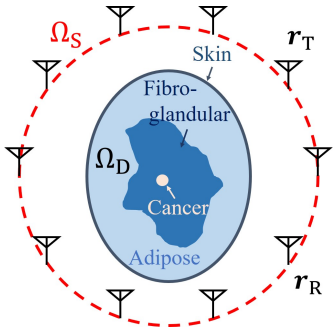

Fig. 1: Observation model. Observation and object areas are defined as $\Omega_{\rm S}$ and $\Omega_{\rm D}$, respectively.

B. Contrast Source Inversion (CSI)

To accomplish an accurate quantitative reconstruction of the complex permittivity of the breast, the CSI method is introduced as a promising IS approach. Derived from the Helmholtz equations, the scattered electric field $E^{\rm S}(\omega;\boldsymbol{r}_{\rm T},\boldsymbol{r}_{\rm R})$ is expressed as:

$$E^{\rm S}(\omega;\boldsymbol{r}_{\rm T},\boldsymbol{r}_{\rm R}) = k_{\rm bg}^2 \int_{\Omega_{\rm D}} G^{\rm bg}(\omega;\boldsymbol{r},\boldsymbol{r}_{\rm R}) w(\omega;\boldsymbol{r}_{\rm T},\boldsymbol{r}) d\boldsymbol{r}, \quad (1)$$

where $k_{\rm bg}$ and $G^{\rm bg}(\omega;\boldsymbol{r},\boldsymbol{r}_{\rm R})$ are the wave number and Green's function of the background media, respectively. $w(\omega;\boldsymbol{r}_{\rm T},\boldsymbol{r}) \equiv \chi(\omega;\boldsymbol{r})E^{\rm T}(\omega;\boldsymbol{r}_{\rm T},\boldsymbol{r})$ is the contrast source, where $\chi(\omega;\boldsymbol{r}) \equiv (\epsilon(\boldsymbol{r})-\epsilon_{\rm bg}(\boldsymbol{r}))/\epsilon_{\rm bg}(\boldsymbol{r})$ is the contrast function, and $\epsilon(\boldsymbol{r})$ and $\epsilon_{\rm bg}(\boldsymbol{r})$ denote the complex permittivities at position $\boldsymbol{r}$ with and without the target, respectively. As a physical constraint, the DIE in (1) must be satisfied in $\Omega_{\rm S}$ and $\Omega_{\rm D}$. Thus, the CSI introduces the following cost function to reconstruct the contrast function $\chi(\omega;\boldsymbol{r})$:

$$F(\chi,w) \equiv \frac{\sum_{\boldsymbol{r}_{\rm T}} \|E^{\rm S}(\omega;\boldsymbol{r}_{\rm T},\boldsymbol{r}_{\rm R}) - \mathcal{G}^S[w]\|^2_{\Omega_{\rm S}}}{\sum_{\boldsymbol{r}_{\rm T}} \|E^{\rm S}(\omega;\boldsymbol{r}_{\rm T},\boldsymbol{r}_{\rm R})\|^2_{\Omega_{\rm S}}} + \frac{\sum_{\boldsymbol{r}_{\rm T}} \|\chi(\boldsymbol{r})E^{\rm I}(\omega;\boldsymbol{r}_{\rm T},\boldsymbol{r}') - w(\omega;\boldsymbol{r}_{\rm T},\boldsymbol{r}) + \chi(\boldsymbol{r})\mathcal{G}^D[w]\|^2_{\Omega_{\rm D}}}{\sum_{\boldsymbol{r}_{\rm T}} \|\chi(\omega;\boldsymbol{r})E^{\rm I}(\omega;\boldsymbol{r}_{\rm T},\boldsymbol{r}')\|^2_{\Omega_{\rm D}}}, \quad (2)$$

Here, $\mathcal{G}^S$ and $\mathcal{G}^D$ are defined as:

$$\mathcal{G}^S[w] = k_{\rm bg}^2 \int_{\Omega_{\rm D}} G^{\rm bg}(\omega;\boldsymbol{r}_{\rm R},\boldsymbol{r}) w(\omega;\boldsymbol{r}_{\rm T},\boldsymbol{r}) d\boldsymbol{r}, (\boldsymbol{r}_{\rm R} \in \Omega_{\rm S}), \quad (3)$$

$$\mathcal{G}^D[w] = k_{\rm bg}^2 \int_{\Omega_{\rm D}} G^{\rm bg}(\omega;\boldsymbol{r}',\boldsymbol{r}) w(\omega;\boldsymbol{r}_{\rm T},\boldsymbol{r}) d\boldsymbol{r}, (\boldsymbol{r}' \in \Omega_{\rm D}), \quad (4)$$

$\|\cdot\|^2_{\Omega_{\rm S}}$ and $\|\cdot\|^2_{\Omega_{\rm D}}$ express the l_2 norms calculated in $\Omega_{\rm S}$ and $\Omega_{\rm D}$, respectively. By sequentially updating $w(\omega;\boldsymbol{r}_{\rm T},\boldsymbol{r})$, $E^{\rm T}(\omega;\boldsymbol{r}_{\rm T},\boldsymbol{r}_{\rm R})$, and $\chi(\omega;\boldsymbol{r})$ (primary unknowns), $F(\chi,w)$ is minimized, and the variable for the total fields in the ROI, $E^{\rm T}(\omega;\boldsymbol{r}_{\rm T},\boldsymbol{r}_{\rm R})$ (secondary unknowns), is also optimized during the CSI processing, which is distinctly characteristic of the CSI scheme.

III. Proposed Method

A. Contrast Source Inversion Enhanced Confocal Imaging (Tomography $\rightarrow$ Radar)

The most used radar imaging approach is based on the coherent integration (CI) scheme, which has been widely employed in microwave breast imaging [5], [6]. Although the CI could reconstruct the reflection coefficient profile with considerably less complexity, compared with the IS

approach, its reconstruction accuracy highly depends on the assumed propagation model, which is mostly set as homogeneous media with average dielectric breast profiles. However, in dealing with highly heterogeneous breast media, the aforementioned presumption generates a nonnegligible erroneous response because of a mismatch between real and assumed dielectric properties. Most studies assume that a clutter response such as skin reflection or heterogeneity-caused scattering is perfectly eliminated during the CI preprocessing, which is hardly possible realistically. This is because a skin reflection waveform generally depends on the breast shape (*e.g.*, the curvature of the surface) or the distance between the element and the skin surface (dielectric coupling effect), which has been demonstrated in some works in the literature [27]–[29] .

To address this, our previous study [9] developed a CSI-based CI scheme, which provides a good estimate of the Green's function in an arbitrary heterogeneous model and generates an accurate clutter signal by exploiting the optimized total fields by the CSI. The methodology is as follows. First, we applied the CSI optimization scheme assuming the background media, such as skin, and adipose-dominant media, *i.e.*, only the total field, $E^{\mathrm{T}}(\omega;\boldsymbol{r}_{\mathrm{T}},\boldsymbol{r})$ is updated using $\hat{\chi}(\omega;\boldsymbol{r})$, which is determined by the assumed background media. Thereafter, by exploiting the aforementioned optimized total field, the Green's function was determined as:

$$\tilde{G}^{\mathrm{bg}}_{\mathrm{T}}(\omega;\boldsymbol{r}_{\mathrm{T}},\boldsymbol{r}) \equiv \frac{\hat{E}^{\mathrm{T}}(\omega;\boldsymbol{r}_{\mathrm{T}},\boldsymbol{r})}{E^{\mathrm{T}}_{\mathrm{bg}}(\omega;\boldsymbol{r}_{\mathrm{T}},\boldsymbol{r}_{\mathrm{T}})} \tag{5}$$

$$\tilde{G}^{\mathrm{bg}}_{\mathrm{R}}(\omega;\boldsymbol{r}_{\mathrm{R}},\boldsymbol{r}) \equiv \frac{\hat{E}^{\mathrm{T}}(\omega;\boldsymbol{r}_{\mathrm{R}},\boldsymbol{r})}{E^{\mathrm{T}}_{\mathrm{bg}}(\omega;\boldsymbol{r}_{\mathrm{R}},\boldsymbol{r}_{\mathrm{R}})} \tag{6}$$

where $E^{\mathrm{T}}_{\mathrm{bg}}(\omega;\boldsymbol{r}_{\mathrm{T}},\boldsymbol{r}_{\mathrm{T}})$ and $E^{\mathrm{T}}_{\mathrm{bg}}(\omega;\boldsymbol{r}_{\mathrm{R}},\boldsymbol{r}_{\mathrm{R}})$ express the total fields measured at $\boldsymbol{r}_{\mathrm{T}}$ from the source at $\boldsymbol{r}_{\mathrm{T}}$ and that measured at $\boldsymbol{r}_{\mathrm{R}}$ from the source at $\boldsymbol{r}_{\mathrm{R}}$, respectively. Also the division operator in (5) and (6) denotes the element-wise division operator along ω. The background media is assumed as a vacuum. $\hat{E}^{\mathrm{T}}(\omega;\boldsymbol{r}_{\mathrm{T}},\boldsymbol{r})$ and $\hat{E}^{\mathrm{T}}(\omega;\boldsymbol{r}_{\mathrm{R}},\boldsymbol{r})$ are the optimized total fields at $\boldsymbol{r}$ by the CSI with the fixed contrast function as $\hat{\chi}(\omega;\boldsymbol{r})$. In addition, $\hat{E}^{\mathrm{T}}(\omega;\boldsymbol{r}_{\mathrm{T}},\boldsymbol{r})$ and $\hat{E}^{\mathrm{T}}(\omega;\boldsymbol{r}_{\mathrm{R}},\boldsymbol{r})$ can be given by the reciprocity theorem, since the transmitters and receivers are convertible.

In addition, the proposed scheme focuses on the following distinct advantage, in terms of clutter signal extraction and suppression. The CSI can provide the total fields in the ROI, which contributes to generating the total fields of the background media (skin and adipose dominant breast) excluding a high contrast object, $\tilde{E}^{\mathrm{TB}}(\omega;\boldsymbol{r}_{\mathrm{T}},\boldsymbol{r}_{\mathrm{R}})$ as :

$$\begin{aligned}\tilde{E}^{\mathrm{TB}}(\omega;\boldsymbol{r}_{\mathrm{T}},\boldsymbol{r}_{\mathrm{R}}) \quad &\equiv \quad E^{\mathrm{I}}(\omega;\boldsymbol{r}_{\mathrm{T}},\boldsymbol{r}_{\mathrm{R}}) \\ +k_{\mathrm{B}}^2\int_{\Omega_{\mathrm{D}}} &\tilde{G}^{\mathrm{B}*}_{\mathrm{R}}(\omega;\boldsymbol{r},\boldsymbol{r}_{\mathrm{R}})\tilde{w}(\omega;\boldsymbol{r}_{\mathrm{T}},\boldsymbol{r})d\boldsymbol{r}, (\boldsymbol{r}_{\mathrm{R}}\in\Omega_{\mathrm{S}}),\end{aligned} \tag{7}$$

$\tilde{G}^{\mathrm{B}*}_{\mathrm{R}}(\omega;\boldsymbol{r}_{\mathrm{R}},\boldsymbol{r})$ is the Green's function in assuming the background media, given by (6). $\tilde{w}(\omega;\boldsymbol{r}_{\mathrm{T}},\boldsymbol{r})$ expresses $\tilde{w}(\omega;\boldsymbol{r}_{\mathrm{T}},\boldsymbol{r}) \equiv \hat{\chi}(\omega,\boldsymbol{r})\hat{E}^{\mathrm{T}}(\omega;\boldsymbol{r}_{\mathrm{T}},\boldsymbol{r})$, where $\hat{\chi}(\omega,\boldsymbol{r})$ is fixed. $\hat{E}^{\mathrm{T}}(\omega;\boldsymbol{r}_{\mathrm{T}},\boldsymbol{r})$ is also provided by the optimization outputs, similar to (5) or (6). Then, the CI image $\tilde{I}(\boldsymbol{r})$ is defined as:

$$\begin{aligned}\tilde{I}(\boldsymbol{r}) \quad &= \quad \sum_{(\boldsymbol{r}_{\mathrm{T}},\boldsymbol{r}_{\mathrm{R}})\in\Omega_{\mathrm{S}}}\int_{-\infty}^{\infty} E^{\mathrm{S}}(\omega;\boldsymbol{r}_{\mathrm{T}},\boldsymbol{r}_{\mathrm{R}}) \\ &\times\tilde{G}^{\mathrm{bg}}_{\mathrm{R}}(\omega;\boldsymbol{r}_{\mathrm{R}},\boldsymbol{r})\tilde{G}^{\mathrm{bg}*}_{\mathrm{T}}(\omega;\boldsymbol{r}_{\mathrm{T}},\boldsymbol{r})d\omega\end{aligned} \tag{8}$$

Details of the aforementioned scheme have been previously described [9]. If we provide a previous background model constituting only skin and adipose tissue (low contrast), the above CI provides the reconstruction image focusing only on high-contrast tissues, such as fibroglandular or cancerous tissues. However, since the CI provides only a qualitative image, such as reflection strength, it is insufficient to discriminate the difference between fibroglandular and tumor tissues. Thus, the post-tomography approach is essentially required for the quantitative reconstruction of complex permittivity to provide an accurate recognition rate between glandular and cancerous tissues.

B. Initial Estimate with Enhanced Confocal Image (Radar → Tomography)

To provide an appropriate initial estimation, this method converts the CI image into the dielectric profile, using the following deconvolution and optimization scheme. Figure 2 illustrates the processing flow of the deconvolution scheme. First, to enhance the spatial resolution of the CI image, the following decomposition is introduced:

$$\hat{I}^{\mathrm{D}}(\boldsymbol{r}) = \iint_{-\infty}^{\infty} H(k_x,k_y;\sigma_{\mathrm{I}};\alpha)e^{j(k_x x+k_y y)}dk_x dk_y \tag{13}$$

where $H(k_x,k_y;\sigma_{\mathrm{I}};\alpha)$ is defined as

$$H(k_x,k_y;\sigma_{\mathrm{I}};\alpha) = W^{\mathrm{Roff}}(k_x,k_y;\alpha)\frac{\tilde{I}(k_x,k_y)}{G(k_x,k_y;\sigma_{\mathrm{I}})} \tag{14}$$

where $\tilde{I}(k_x,k_y)$ denotes the 2-D Fourier transform of $\tilde{I}(\boldsymbol{r})$ in terms of x and y. $G(k_x,k_y;\sigma_{\mathrm{I}})$ is defined as :

$$G(k_x,k_y;\sigma_{\mathrm{I}}) = \iint_{-\infty}^{\infty}\exp\left[-\frac{(x^2+y^2)}{2\sigma_{\mathrm{I}}^2}\right]e^{-j(k_x x+k_y y)}dxdy \tag{15}$$

where σ_{I} denotes the standard deviation of the Gaussian point spread function. In addition, $W^{\mathrm{Roff}}(k_x,k_y;\alpha)$ is the roll-off filter based windowing function as follows:

[Eq.(12) is in the head note.]

where $k_r \equiv \sqrt{k_x^2+k_y^2}$ holds. Parameters σ_{I} and α are determined by considering the point spread function and side-lobe level of the output image $\hat{I}^{\mathrm{D}}(\boldsymbol{r})$, assuming a single point object in the background media.

The initial estimate of the Debye parameter profiles are determined as follows:

$$\boldsymbol{p}(\boldsymbol{r};\beta) = \boldsymbol{p}_{\mathrm{B}}(\boldsymbol{r}) + \beta\tilde{I}(\boldsymbol{r})\boldsymbol{p}_{\mathrm{tumor}} \tag{16}$$

where $\boldsymbol{p}_{\mathrm{canc}} \equiv (\epsilon_{\infty}^{\mathrm{tumor}},\Delta\epsilon^{\mathrm{tumor}},\sigma_{\mathrm{s}}^{\mathrm{tumor}})$ denotes the representative Debye parameter vector of the tumor tissue. $\boldsymbol{p}_{\mathrm{canc}}(\boldsymbol{r}) \equiv (\epsilon_{\infty}^{\mathrm{tumor}},\Delta\epsilon^{\mathrm{tumor}},\sigma_{\mathrm{s}}^{\mathrm{tumor}})$ is defined as:

$$\boldsymbol{p}_{\mathrm{B}}(\boldsymbol{r}) \equiv \begin{cases}(\epsilon_{\infty}^{\mathrm{skin}},\Delta\epsilon^{\mathrm{skin}},\sigma_{\mathrm{s}}^{\mathrm{skin}}), (\boldsymbol{r}\in\Omega_{\mathrm{skin}}\cap\Omega_{\mathrm{D}}) \\ (\epsilon_{\infty}^{\mathrm{adi}},\Delta\epsilon^{\mathrm{adi}},\sigma_{\mathrm{s}}^{\mathrm{adi}}), (\boldsymbol{r}\in\overline{\Omega}_{\mathrm{skin}}\cap\Omega_{\mathrm{D}})\end{cases} \tag{17}$$

$$W^{\mathrm{Roff}}(k_x,k_y;\alpha)=\begin{cases}1, & (0\le k_r\le(1-\alpha)k_r^{\mathrm{th}})\\ \frac{1}{2}\left\{1-\sin\left(\frac{\pi(k_r-k_r^{\mathrm{th}})}{2\alpha k_r^{\mathrm{th}}}\right)\right\}, & ((1-\alpha)k_r^{\mathrm{th}}<k_r\le(1+\alpha)k_r^{\mathrm{th}})\\ 0, & (k_r>(1+\alpha)k_r^{\mathrm{th}})\end{cases} \tag{12}$$

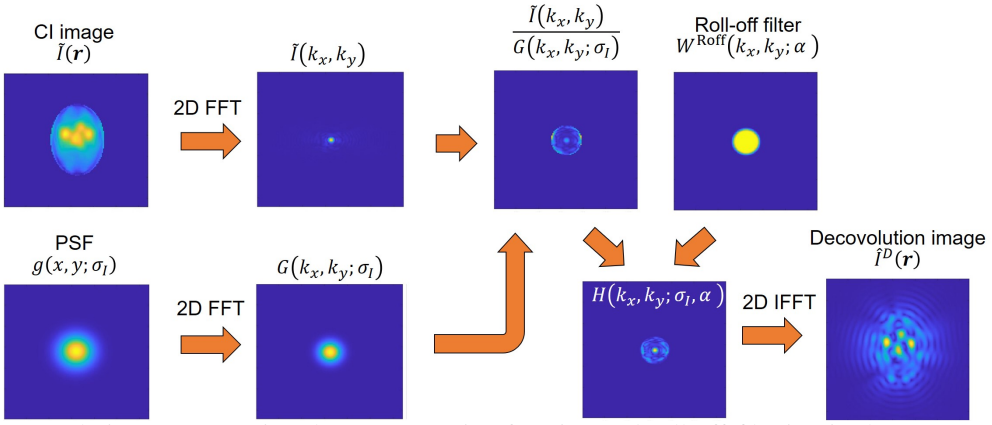

Fig. 2: Deconvolution process using the 2-D Gaussian function and roll-off filtering in the proposed method.

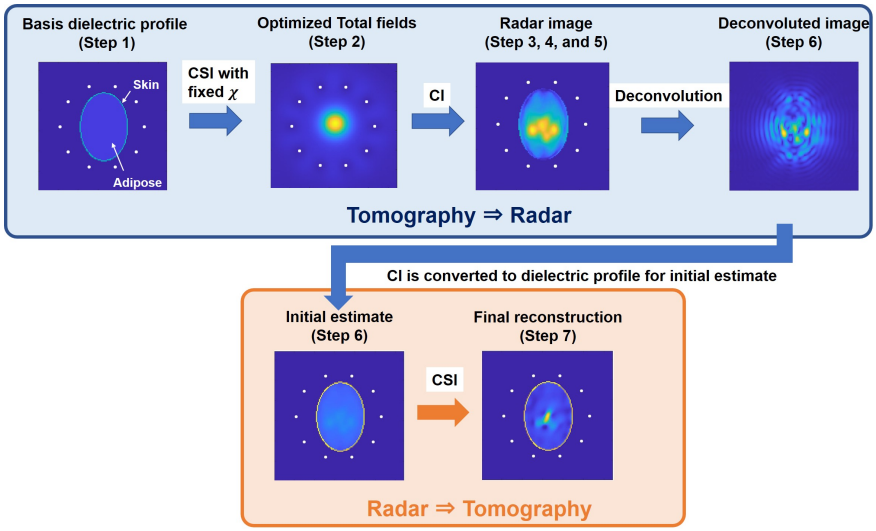

Fig. 3: Schematic diagram of the proposed method. Bi-directional processing between radar and tomography.

Notably, since we assume that the background media are composed of only skin and adipose tissue, the parameters for fibroglandular, or cancer tissues are not required here.

Parameter β is then, optimized as:

$$\hat{\beta}=\arg\min_{\beta} F(\chi(\boldsymbol{p}(\boldsymbol{r};\beta)),\omega) \tag{18}$$

Here $\chi(\boldsymbol{p}(\boldsymbol{r};\beta))$ denotes the contrast function, which is defined by the given Debye profile $\boldsymbol{p}(\boldsymbol{r};\beta)$. Finally, the initial estimate is determined as $\chi(\boldsymbol{p}(\boldsymbol{r};\hat{\beta}))$, and the CSI iteration process is conducted with N iterations to provide a final reconstruction profiles of the complex permittivity. Note that, this study does not focus on the resolution enhancement for the CI images, but aims at to provide an accurate initial estimate using higher resolutions and more accurate CI profiles, for the post-quantitative imaging with CSI.

C. Procedure of Proposed Method

Figure 3 shows the schematic diagram of the proposed method, namely, the bi-directional processing between radar and tomography. The procedure of this method is as follows:

Step 1): The dielectric profile using only skin and adipose media is defined in (17) as $\boldsymbol{p}_{\mathrm{B}}(\boldsymbol{r})$, and $\chi^{\mathrm{low}}(\omega,\boldsymbol{r})$ is also defined using this profile as $\boldsymbol{p}_{\mathrm{B}}(\boldsymbol{r})$, assuming that the background media is a vacuum.

Step 2): $\hat{E}^{\mathrm{T}}(\omega;\boldsymbol{r}_{\mathrm{T}},\boldsymbol{r})$ is optimized at each angular frequency ω, by minimizing the CSI cost function in (2), where $\chi^{\mathrm{low}}(\omega,\boldsymbol{r})$ is fixed in the iteration process.

Step 3): The Green's functions, $\tilde{G}^{\mathrm{B}}_{\mathrm{T}}(\omega;\boldsymbol{r}_{\mathrm{T}},\boldsymbol{r})$ and $\tilde{G}^{\mathrm{B}}_{\mathrm{R}}(\omega;\boldsymbol{r}_{\mathrm{R}},\boldsymbol{r})$, are determined in (5) and (6), respectively, by the updated total field as $\hat{E}^{\mathrm{T}}(\omega_i;\boldsymbol{r}_{\mathrm{T}},\boldsymbol{r})$.

Step 4): The clutter signal, $\tilde{E}^{\mathrm{TB}}(\omega_i;\boldsymbol{r}_{\mathrm{T}},\boldsymbol{r}_{\mathrm{R}})$, is generated by ((7)), and is eliminated from the scattered signal. The scattered field is determined, assuming a multi-layered background $\tilde{E}^{\mathrm{S}}(\omega_i;\boldsymbol{r}_{\mathrm{T}},\boldsymbol{r}_{\mathrm{R}})$.

Step 5): The CSI-enhanced CI process is conducted using (8) and generates the image as $\tilde{I}(\boldsymbol{r})$.

Step 6): Image deconvolution is applied in (13), and the

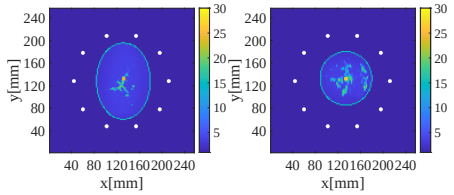

(a) ϵ_∞ of Class 1 (b) ϵ_∞ of Class 2

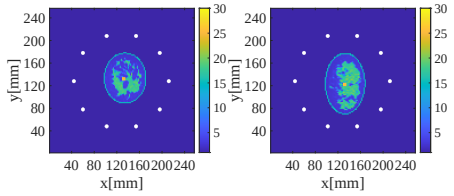

(c) ϵ_∞ of Class 3 (d) ϵ_∞ of Class 4

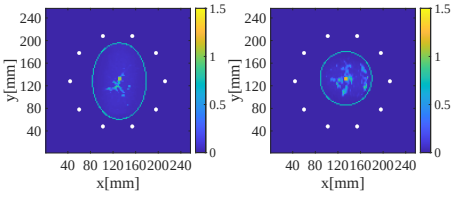

(e) σ_s of Class 1 (f) σ_s of Class 2

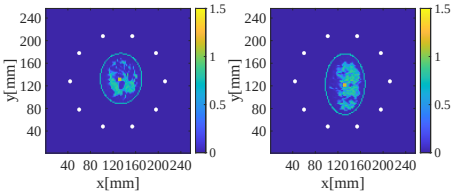

(g) σ_s of Class 3 (h) σ_s of Class 4

Fig. 4: Ground truth profiles of Debye parameters ϵ_∞ and σ_s in each class. White dots denote the transmitters and receivers.

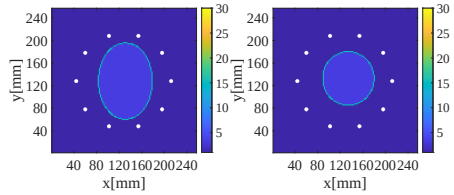

(a) ϵ_∞ of Class 1 (b) ϵ_∞ of Class 2

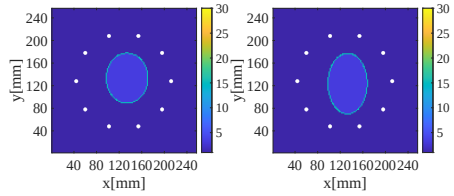

(c) ϵ_∞ of Class 3 (d) ϵ_∞ of Class 4

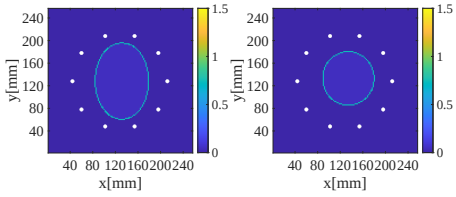

(e) σ_s of Class 1 (f) σ_s of Class 2

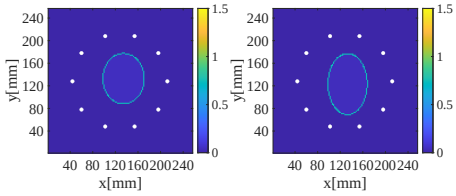

(g) σ_s of Class 3 (h) σ_s of Class 4

Fig. 5: Background profile composed of adipose and skin tissue as to the Debye parameters ϵ_∞ and σ_s in each class. White dots denote the transmitters and receivers.

initial estimate for the Debye parameters are determined as $\chi(\boldsymbol{p}(\boldsymbol{r};\hat{\beta}))$ using (18).

Step 7): Using the initial estimate, $\chi(\boldsymbol{p}(\boldsymbol{r};\hat{\beta}))$, CSI is applied and affords the final reconstruction profile of complex permittivity.

Notably, Step 3 generates the accurate propagation model for heterogeneous media, and Step 4 introduces the suppression process for the clutter from the skin surface.

IV. Numerical Test

A. Numerical setup

The 2-D FDTD based numerical investigations are described as follows. This simulation introduces the four types of MRI-derived phantoms as : Class 1 (mostly fatty, ID = 012804), Class 2 (scattered fibroglandular, ID = 070604PA1); Class 3 (heterogeneously dense, ID = 062204); and Class 4 (very dense, ID = 012304); which are available from published repositories [30]. The frequency dispersion model is expressed as the single-pole Debye as follows:

$$\epsilon_{\mathrm{Debye}}(\omega;\epsilon_\infty,\Delta\epsilon,\sigma_\mathrm{s}) = \varepsilon_\infty + \frac{\Delta\varepsilon}{1+j\omega\tau} + \frac{\sigma_\mathrm{s}}{j\omega\varepsilon_0}, \qquad (19)$$

where τ is the relaxation time, and is fixed at $\tau = 1.5\times10^{-11}$ s. The main Debye parameters $(\epsilon_\infty, \Delta\epsilon, \sigma_\mathrm{s})$ could be accurately associated with the MRI image via piece-wise linear mapping [31]. Then, the scattered data are generated using the 2-D FDTD, where the above single pole Debye dispersion model is introduced. Figure 4 illustrates the spatial profile for two of the Debye parameters as ϵ_∞ and σ_s of four different phantoms, and Table I shows the assumed range for the Debye parameters of each tissue, which is dependent on the associated MRI image strength. Cancerous tissue with dimensions of 6mm $\times$ 6mm is located at the center of each phantom, with the Debye parameters of $(\epsilon_\infty, \Delta\epsilon, \sigma_\mathrm{s}) = (22.0, 51.6, 1, 3)$, derived from a previous study [31]. The 10 transmitters (ideal point sources) and receivers configures a circular array, and all their combination data are input into the inversion scheme. The Gaussian modulated pulse with 1.27 GHz center frequency and 1.91 GHz bandwidth is excited as the source current. All the cell sizes of the FDTD, CI and CSI are unified as 2 mm, where the FDTD code was modified from the original in-house code by the University of Wisconsin Madison.

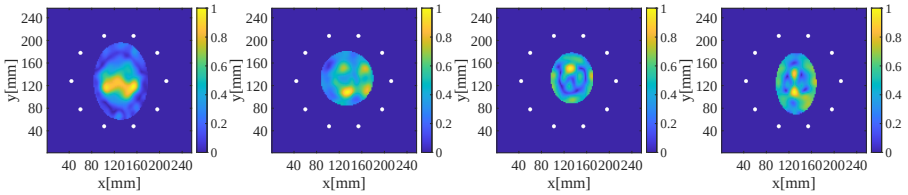

(a) Class 1 : $\epsilon_{\rm bg} = 6$ (b) Class 2 : $\epsilon_{\rm bg} = 6$ (c) Class 3 : $\epsilon_{\rm bg} = 6$ (d) Class 4 : $\epsilon_{\rm bg} = 6$

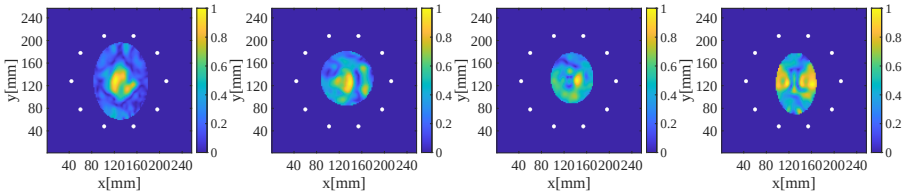

(e) Class 1 : $\epsilon_{\rm bg} = 8$ (f) Class 2 : $\epsilon_{\rm bg} = 8$ (g) Class 3 : $\epsilon_{\rm bg} = 8$ (h) Class 4 : $\epsilon_{\rm bg} = 8$

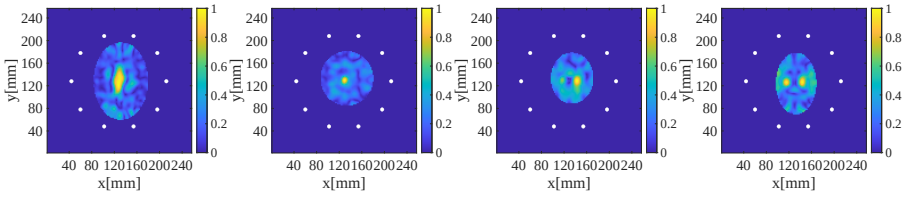

(i) Class 1 : $\epsilon_{\rm bg} = 10$ (j) Class 2 : $\epsilon_{\rm bg} = 10$ (k) Class 3 : $\epsilon_{\rm bg} = 10$ (l) Class 4 : $\epsilon_{\rm bg} = 10$

Fig. 6: Reconstruction images by the conventional CI method for each class at the two conditions.

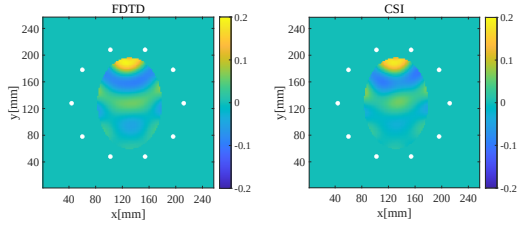

(a) Real part

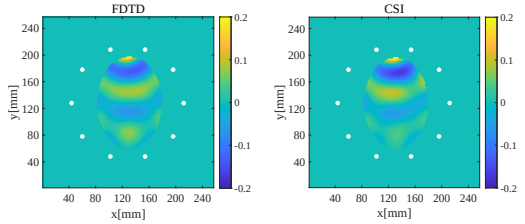

(b) Imaginary part

Fig. 7: Reconstruction profile of the total field in the ROI area at the specific transmitter at Class 1 and the frequency at 1.27 GHz.

TABLE I: Debye parameters for each tissue.

Tissue type	ϵ_∞	$\Delta\epsilon$	$\sigma_{\rm s}$ [S/m]
Skin	15.9	23.8	0.83
Adipose (median)	3.1	1.6	0.05
Fibroglandular (median)	13.8	35.6	0.74
Fibroglandular (high)	18.3	43.0	1.08
Cancer	22.0	51.6	1.30

B. Results : Tomography → Radar (CSI enhanced CI)

First, the CI image reconstruction is presented. We first assume a noiseless situation to assess the systematical error in each process. For the method comparison, the traditional CI results are introduced, which assumes that the breast media forms a homogeneous profile with the representative complex permittivity [9]. Here, for clutter suppression in the traditional and proposed CI schemes, we assume a simple breast model comprising only skin and adipose media, as shown in Fig. 5. Figure 6 shows the results obtained from the CI images, where the three different relative permittivities are assumed to be $\epsilon_{\rm bg} = 6, 8$, and 10, because the reconstruction accuracy of the CI image is mostly dependent on the relative permittivity $\epsilon_{\rm bg}$, which is converted to the propagation speed $v_{\rm bg}$ in the breast media as $v_{\rm bg} = v_{\rm air}/\sqrt{\epsilon_{\rm bg}}$ with that in the air as $v_{\rm air}$. Here, all the imaging areas, in Figure 6, are truncated on the boundary between the skin of the breast and air. Notably, in the traditional CI image, the clutter signal from the background media (Fig. 5), is generated in the FDTD, and eliminated. As shown in Fig. 6, the traditional CI image could not provide an accurate location or area of the high contrast object of fibro-glandular or cancer tissues, which are mainly caused by a mismatch in the relative permittivity.

TABLE II: Details of each condition of the proposed method.

	Green's functions in (5) and (6))	Total fields in (7)
Cond. I	FDTD	FDTD
Cond. II	CSI	CSI

Next, the reconstruction results of the CSI enhanced CI is presented as follows. In this case, we investigate the two conditions, with regard to calculation of the Green's function in (5) and (6) and the clutter suppression in (7). In Cond. I, the total fields $\hat{E}^{\rm T}(\omega, \boldsymbol{r}; \boldsymbol{r}_{\rm T})$ and the scattered fields $\tilde{E}^{\rm S}(\omega; \boldsymbol{r}_{\rm T}, \boldsymbol{r}_{\rm R})$ are given by the FDTD method; that

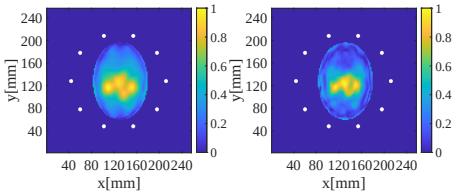

(a) Class 1 : Cond. I (b) Class 1 : Cond. II

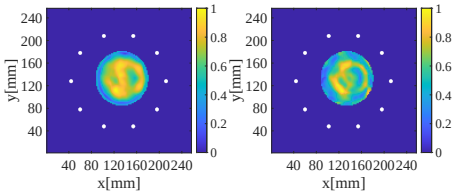

(c) Class 2 : Cond. I (d) Class 2 : Cond. II

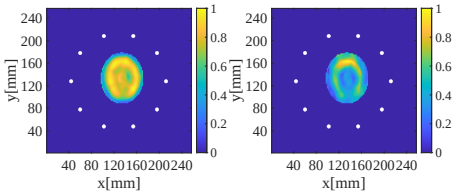

(e) Class 3 : Cond. I (f) Class 3 : Cond. II

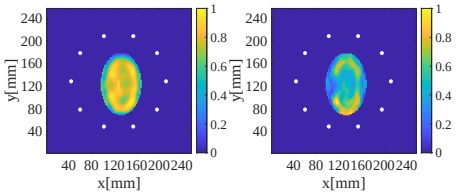

(g) Class 4 : Cond. I (h) Class 4 : Cond. II

Fig. 8: Reconstruction images by the proposed CI method for each class at the two conditions.

is, the ideal case, where an referential information is input to the enhanced SAR reconstruction in (8). On the contrary, in Cond. II , $\tilde{E}^{\mathrm{S}}(\omega; \boldsymbol{r}_{\mathrm{T}}, \boldsymbol{r}_{\mathrm{R}})$ and $\hat{E}^{\mathrm{T}}(\omega, \boldsymbol{r}; \boldsymbol{r}_{\mathrm{T}})$ are calculated by the optimization output of the CSI. Here, the convergence criteria of the above CSI process is determined by the maximum iteration number, which is set to 1000 in this case. Table II summarizes the definitions of these conditions. Figure 7 illustrates the reconstruction results of the total fields in the ROI cells at the specific transmitter, compared with the FDTD data, and it demonstrates that the CSI can optimize the total field in all ROI cells with considerable similarity to that provided by the FDTD, (*i.e.*, reference data). Thus, the Green's functions in (5) and (6) could be accurately provided for post CI processes.

Next, Fig. 8 shows the reconstruction results using the proposed method in both Cond. I and II, where each imaging area is truncated on the boundary between the skin of the breast and air. As shown in the results in Fig. 8, the proposed CI schemes reconstruct the high energy around the boundary area between the adipose and fibroglandular areas, because the main reflection inside the breast is caused by the contrast between the these tissues. Although the cancerous tissues are buried in the responses of the fibroglandular area, it provides

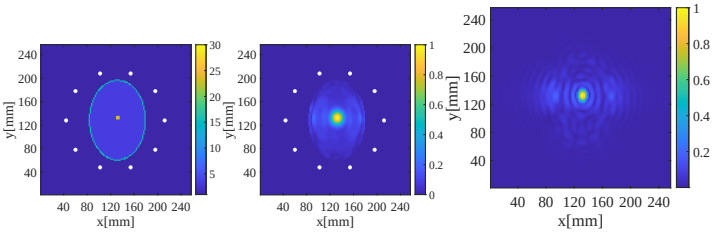

(a) True ϵ_∞ (b) CI w/o deconv. (c) CI w/ deconv.

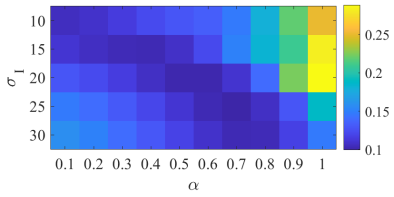

(d) $\mathrm{Err}_{\mathrm{CI}}(\sigma_{\mathrm{I}}, \alpha)$

Fig. 9: Determination of the optimal α and σ_{I} by evaluating the point-spread function.

an appropriate initial estimate for the post-CSI quantitative imaging to distinguish the tumor and fibro-tissues based on the dielectric profile. In addition, the CI images in Cond. II has a differential response from Cond. I, that is, the referential CI image, because of inaccuracy for generating the total field in the ROI area. These differences are more distinct in the dense cases, such as Class 3 or 4, and this is because a high contrast profile requires more iteration numbers to reach the certain accuracy of total field optimization.

C. Results : Radar → Tomography (CI enhanced CSI)

1) Deconvolution Results: Here, the CI enhanced CSI approach is investigated as follows. First, the initial estimate scheme using the CI image with the Gaussian function based deconvolution is assessed as follows. In this case, parameters σ_{I} and α used in (13) are optimized under the criteria with the following root mean square errors (RMSE) between the ground truth profile and the output CI images as:

$$\mathrm{Err}_{\mathrm{CI}}(\sigma_{\mathrm{I}}, \alpha) = \frac{1}{N_{\mathrm{I}}} \sqrt{\frac{\sum_{i=1} |I_{\mathrm{true}}(\boldsymbol{r}_i) - \tilde{I}(\boldsymbol{r}_i)|^2}{\sum_{i=1} |I_{\mathrm{true}}(\boldsymbol{r}_i)|^2}} \tag{20}$$

Although the metric $\mathrm{Err}_{\mathrm{CI}}(\sigma_{\mathrm{I}}, \alpha$ does not directly evaluate the spatial resolution of the radar image, it can assess the accuracy for the initial estimate of the post-CSI processing, that is, the similarity to the actual dielectric profile. Figure 9 shows the evaluations of the aforementioned errors $\mathrm{Err}_{\mathrm{CI}}(\sigma_{\mathrm{I}}, \alpha)$ as a function of σ_{I} and α assuming that the single point-shape object $(\epsilon_\infty, \Delta\epsilon, \sigma_{\mathrm{s}}) = (23.3, 43.0, 1.03)$ is located in the center of the breast with a skin-adiposed based background in the Class 1. This figure shows that there is an optimal combination of these parameters at the minimal RMSE, and we determine that the optimal parameters of $\hat{\sigma}_{\mathrm{I}}$ and $\hat{\alpha}$ are 50 mm and 0.7, respectively. Note that, this target model corresponds to the PSF. While we cannot optimize the parameters for unknown arbitrary breast profiles, a general radar image, including a response from fibro-glandular or cancer tissues, is generally approximated as a convolution image between the actual contrast function profile $\chi(\boldsymbol{r})$ and

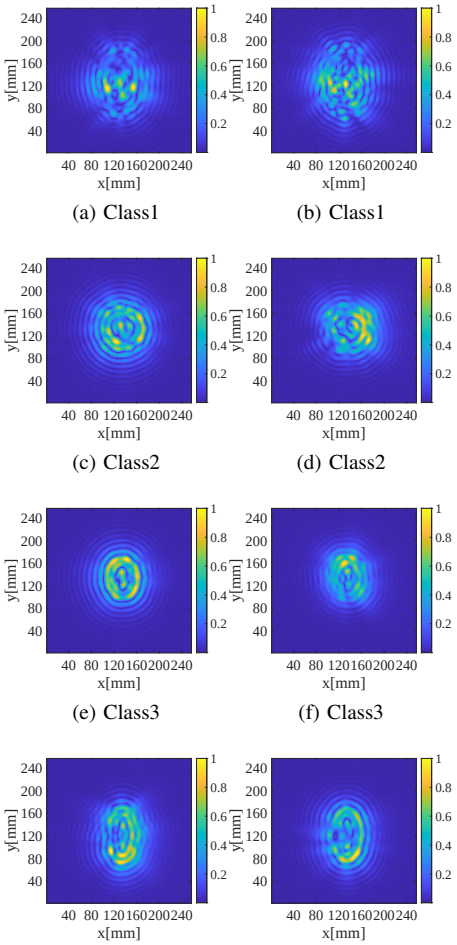

(a) Class1 (b) Class1

(c) Class2 (d) Class2

(e) Class3 (f) Class3

(g) Class4 (h) Class4

Fig. 10: Deconvolution results of the CSI-enhanced CI images for each class. 1st line: Cond. I. 2nd line: Cond. II.

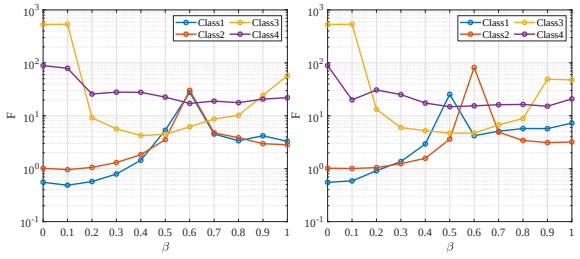

(a) Cond. I (b) Cond. II

Fig. 11: Cost function as a function of β in each class.

the PSF. Thus, we use the optimal parameter in assuming the above PSF model in the following analysis. Figure 10 shows the deconvolution results of the CI images of Fig. 8 using the optimal parameters of $\hat{\sigma}_{\mathrm{I}}$ and $\hat{\alpha}$ for both Conditions I and II. The results in Figure 10 demonstrate that the deconvolution scheme in Sec. III-B successfully upgrades the spatial resolution of the CI images, which contributes to the post-initial estimation process. Although some sidelobe responses are appeared outside area of the breast area, which could be truncated from the ROI. In addition, this approach is based on the linear approximation, and there are also some unnecessary responses due to the non-linear effect.

2) Reconstruction Results: As the next step described in 18, the initial estimate for the post CSI reconstruction is determined using the deconvoluted CI image as in Fig. 10. Figure 11 shows the minimized CSI cost function for each selected β defined in (18) for each Condition. Table III summarizes the optimized parameters $\hat{\beta}$ using 18 in each class. In the case of Class 1 or 2, namely, the lower density of the fibroglandular area, a low β is selected as the optimal value because the adipose area with a low dielectric contrast is dominant either class. Contrarily, focusing on Class 3 or 4, *i.e.*, highly heterogeneous media, a high β becomes an optimal because the initial estimate should have a high contrast profile, and those effects are almost common in Cond. I and II.

TABLE III: Optimized β in determining the initial estimate with CSI cost function.

	Class 1	Class 2	Class 3	Class 4
Cond. I	0.1	0.1	0.4	0.6
Cond. II	0.1	0.1	0.5	0.5

TABLE IV: RMSE of real part of complex permittivity @ 1.27 GHz, in each class and method.

	Original CSI	Proposed CSI		
		$\beta = 0$	Cond. I $\beta = \tilde{\beta}$	Cond. II $\beta = \tilde{\beta}$
Class 1	8.82	5.16	5.13	5.18
Class 2	10.89	8.14	8.08	8.21
Class 3	24.56	23.50	12.67	12.71
Class 4	25.86	24.52	16.50	15.30

Figures 12 and 13 show the initial estimate using each $\hat{\beta}$ in (16), as to the two of Debye parameters as ϵ_∞ and σ_{s}, respectively. Figures 12 and 13 show that the proposed scheme could provide an appropriate initial estimate in each class, which is exploited in the CSI reconstruction. Figs. 14 and 15 show the reconstruction results of complex permittivity for real and imaginary parts, respectively, in each method, and condition. Focusing on the result in the original CSI, that is, without using the CI based initial estimate, it considerably suffers from inaccuracy especially for in highly heterogeneous models as Class 3 or 4, because the optimized solution in the original CSI would fall into the local optimal by starting from vacuum based initial estimates, and could not reach the global optimum, particular for the area with high contrast function. The results in Figs. 14 and 15 also confirm that the accuracy of the reconstruction results using the proposed method is significantly enhanced by those obtained using the original CSI scheme, by starting from more accurate initial estimate, especially in Class 3 and 4. Tables IV and V shows the quantitative error analysis for the reconstruction results, with the RMSEs for each real and imaginary part of the complex permittivity at 1.27 GHz. The results in Tables IV and V also demonstrated that the proposed approach considerably suppress the RMSE values. Note that, the accuracy improvement in Class 1 and 2 is limited compared with those obtained at the case of $\beta = 0$, because it starts the initial estimate with lower β as in Table III. On the contrary, in the cases of Class 3 or 4, namely, a highly heterogeneous profile, the initial estimate with higher

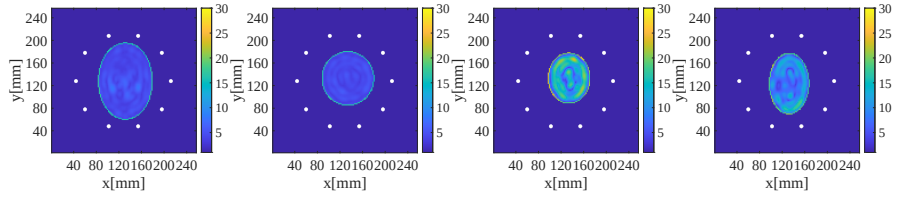

(a) Class1 (Cond. I) (b) Class2 (Cond. I) (c) Class3 (Cond. I) (d) Class4 (Cond. I)

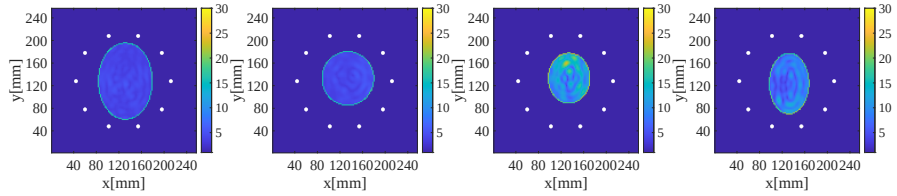

(e) Class1 (Cond. II) (f) Class2 (Cond. II) (g) Class3 (Cond. II) (h) Class4 (Cond. II)

Fig. 12: Initially estimated permittivity profile as to ϵ_∞ for each class and condition. 1st line: Cond. I. 2nd line: Cond. II.

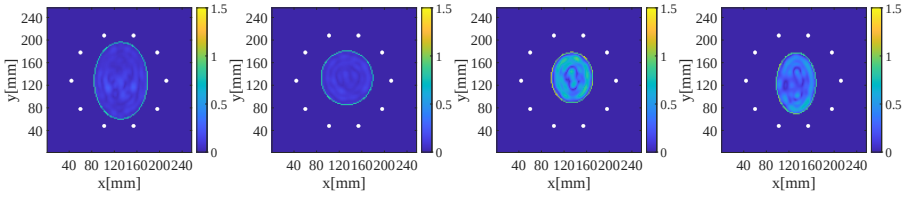

(a) Class1 (Cond. I) (b) Class2 (Cond. I) (c) Class3 (Cond. I) (d) Class4 (Cond. I)

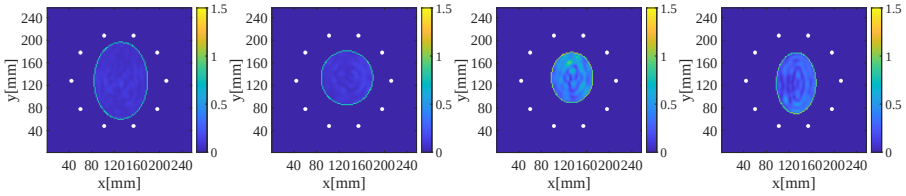

(e) Class1 (Cond. II) (f) Class2 (Cond. II) (g) Class3 (Cond. II) (h) Class4 (Cond. II)

Fig. 13: Initially estimated permittivity profile as to $\sigma_{\rm s}$ for each class and condition. 1st line: Cond. I. 2nd line: Cond. II.

TABLE V: RMSE of imaginary part of complex permittivity @ 1.27 GHz, in each class and method.

	Original CSI	Proposed CSI		
		$\beta = 0$	Cond. I $\beta = \tilde{\beta}$	Cond. II $\beta = \tilde{\beta}$
Class 1	2.98	1.80	1.71	1.72
Class 2	4.08	3.18	3.01	3.08
Class 3	9.59	9.52	6.44	6.70
Class 4	18.1	20.08	8.68	8.03

β contributes to accuracy improvement, compared with those obtained by $\beta = 0$, that is the advantage of the processing in Sec. III-B.

3) Error Analysis: As another quantitative analysis, the correlation coefficients, denoted as $\rho_{\rm re}$ and $\rho_{\rm im}$ between true and reconstructed profiles, for both real and imaginary parts of complex permittivity, are introduced as:

$$\rho_{\rm re} = \frac{\boldsymbol{\epsilon}^{\Re}_{\rm true} \cdot \boldsymbol{\epsilon}^{\Re}_{\rm est}}{\|\boldsymbol{\epsilon}^{\Re}_{\rm true}\| \|\boldsymbol{\epsilon}^{\Re}_{\rm true}\|} \tag{21}$$

$$\rho_{\rm im} = \frac{\boldsymbol{\epsilon}^{\Im}_{\rm true} \cdot \boldsymbol{\epsilon}^{\Im}_{\rm est}}{\|\boldsymbol{\epsilon}^{\Im}_{\rm true}\| \|\boldsymbol{\epsilon}^{\Im}_{\rm true}\|} \tag{22}$$

where $\boldsymbol{\epsilon}^{\Re}_{\rm true}$ and $\boldsymbol{\epsilon}^{\Re}_{\rm est}$ denote the spatial profile of the real part of complex permittivity of the ground truth and reconstructed images, respectively. $\boldsymbol{\epsilon}^{\Im}_{\rm true}$ and $\boldsymbol{\epsilon}^{\Im}_{\rm est}$ also denote those of the imaginary parts of complex permittivity of the ground truth and reconstructed images, respectively. The indexes $\rho_{\rm re}$ and $\rho_{\rm im}$ quantitatively assesses the similarity between true and estimated profiles, especially for a similarity of area with higher contrast, that is, a cancer and fibroglandular area. Tables VI and VII show the evaluations of $\rho_{\rm re}$ and $\rho_{\rm im}$ for each method, and demonstrate that our proposed scheme significantly enhances the similarity of dielectric profile, compared with those obtained by the original CSI scheme and the case without using the CI image ($\beta = 0$) in the initial estimate, in particular of Class 3 or 4. There are some negative values in $\rho_{\rm re}$ (*e.g.*, the original CSI in Tables VI), and it is predicted that there are many cells with an inverse relationship between true and reconstructed dielectric properties. Note that, the accuracy of the imaginary part in Class 3 or 4 is relatively lower than those of the real part. This is because these classes have high lossy media with densely distributed fibroglandular tissues, which makes difficult to extract the scattered signal from deeper area of breast media.

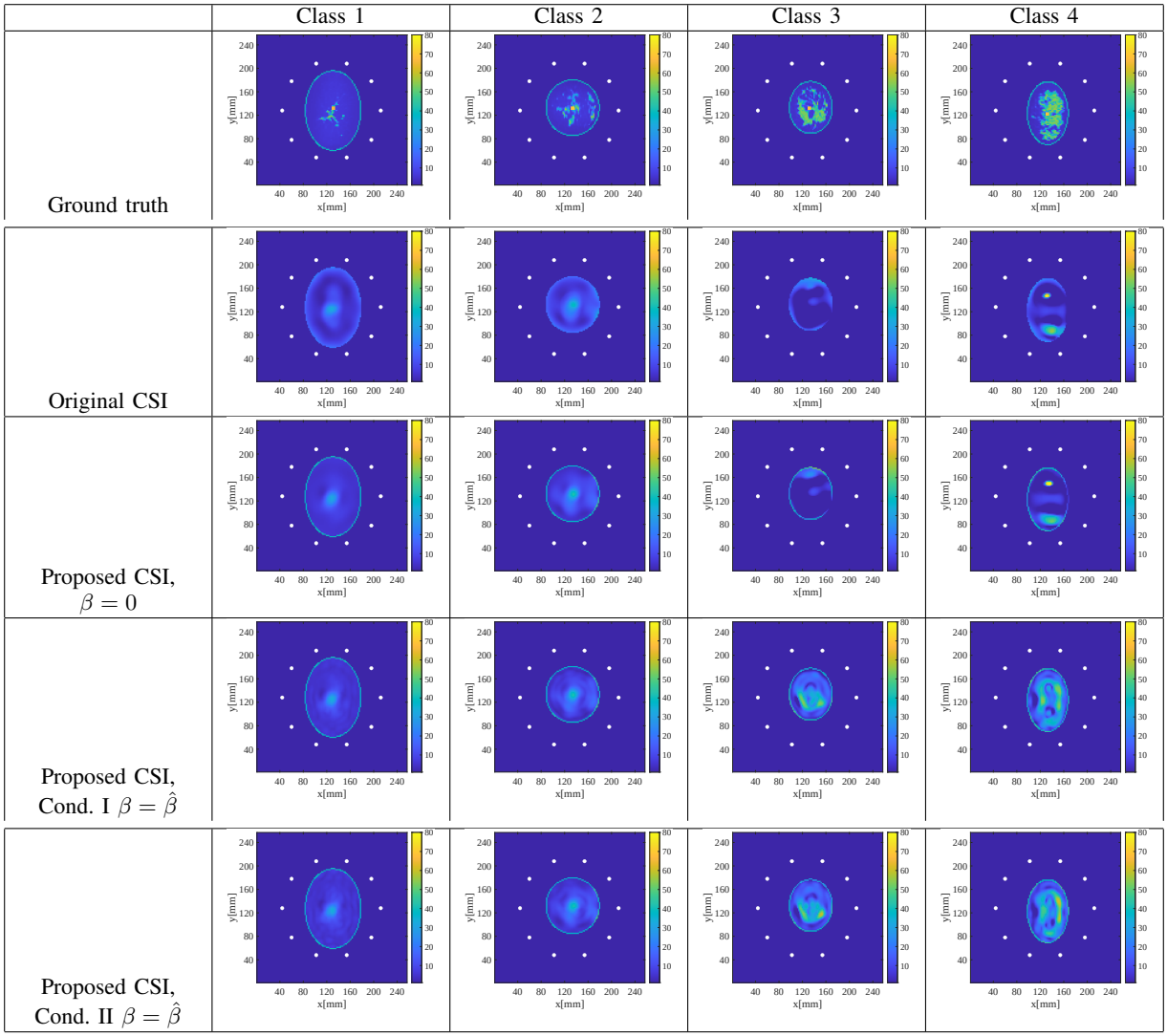

Fig. 14: Reconstruction results for real part of the complex permittivity at 1.27 GHz in each method and Class.

TABLE VI: ρ_{re} @ 1.27 GHz, in each class and method.

	Original CSI	Proposed CSI		
		$\beta = 0$	Cond. I $\beta = \tilde{\beta}$	Cond. II $\beta = \tilde{\beta}$
Class 1	0.553	0.873	0.875	0.873
Class 2	0.574	0.790	0.793	0.785
Class 3	-0.060	0.213	0.743	0.740
Class 4	0.098	0.300	0.563	0.637

TABLE VII: ρ_{im} @ 1.27 GHz, in each class and method.

	Original CSI	Proposed CSI		
		$\beta = 0$	Cond. I $\beta = \tilde{\beta}$	Cond. II $\beta = \tilde{\beta}$
Class1	0.563	0.867	0.881	0.880
Class2	0.404	0.689	0.726	0.714
Class3	0.094	0.235	0.368	0.320
Class4	0.083	0.214	0.254	0.227

4) Case for Different Cancer Locations: Notably, our proposed scheme does not assume nor use prior knowledge of the cancer location. To demonstrate the above, we investigate the cases with different cancer cell locations located at off-center areas of the breast. Here, as a representative model for lowly and highly dense breasts, the Class 1 and 4 are investigated as follows. Figure 16 shows the reconstruction results of the CSI enhanced CI image and its deconvolution image, which could offer accurate focus on the actual cancer positions, especially for the Class 1 model. Figure 17 also shows the reconstruction results obtained by the original CSI (without CI prior) and the proposed CSI method, where the Condition II is assumed. In this case, the optimized β for Classes 1 and 4 are 0.1 and 0.6, respectively. These results demonstrated that our proposed scheme is applicable to different locations of the cancer tissues, as any prior knowledge of the cancer location is not used in both the CI and CSI processing schemes.

TABLE VIII: RMSE and ρ in each class and method at the off-centered cancer case.

	Class	RMSE		ρ	
		$\Re[\epsilon]$	$\Im[\epsilon]$	$\Re[\epsilon]$	$\Im[\epsilon]$
Original CSI	Class 1	8.96	3.08	0.54	0.52
	Class 4	25.99	17.26	0.14	0.15
Proposed CSI	Class 1	5.41	1.67	0.86	0.87
	Class 4	14.50	7.67	0.68	0.27

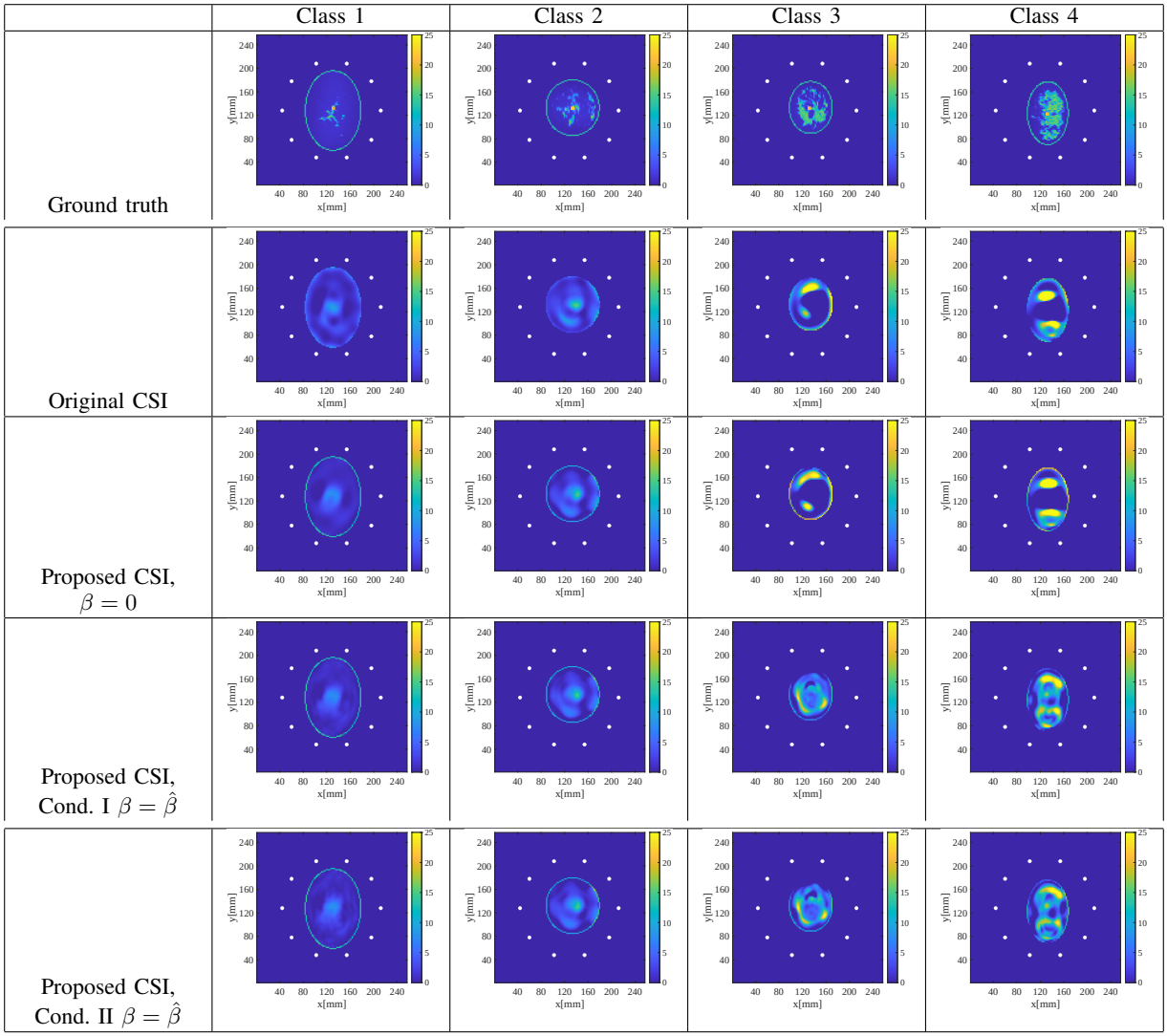

Fig. 15: Reconstruction results for imaginary part of the complex permittivity at 1.27 GHz in each method and Class.

D. Case for Additive Noise

In this section, the case with additive noise is investigated to assess the sensitivity to noisy components. In this simulation model, the cell sizes in both the forward and inverse problems are set to the same dimension as 2 mm, which might incur the so-called inverse crime as in [32]. However, in some previous works [32], this issue would be mitigated, by considering the situation with additive noise as follows. White Gaussian noises are added to the observed total fields in the time domain. The signal-to-noise ratio (SNR) is determined as the ratio of maximum signal to noise power (variance of the Gaussian distribution, and the signal includes reflection responses from the skin surface, which would be much stronger than those from the inner area of the breast, such as fibro-glandular, or cancer tissues, because we do not assume a matching coupling media to suppress the skin reflection. As in Sec. IV-C4, the two representative cases as Class 1 and 4 are investigated as follows. We assume the two cases as having SNR values of 30 and 40 dB, respectively. While these SNR levels are apparently high, they are available in the actual measurement scenario, such as in [29], Figure 18 shows an example of the received signal assuming the Class 1 at each SNR level, where the responses with, or without skin reflection elimination are illustrated for a noise-free situation. This figure shows that the response from the inner area (yellow) is considerably less than that of skin reflection (red), and is buried into the noise component, especially for an SNR of 30 dB. Notably, if we calculate the SNR using only signals from the inner area, the actual SNR levels of Fig. 18 (a) and (b) are estimated to be 4 dB and 14 dB, respectively; that is, their powers are -26 dB less than that of skin reflection. Figures 20 and 19 show the qualitative radar images by the CSI enhanced CI and its deconvolution image, and illustrates the quantitative tomography images by the original and the proposed CSI methods, at the SNR levels of 30 and 40 dB, respectively. Table IX summarizes the RMSEs and ρ for each reconstructed real and imaginary parts of complex permittivity. As shown in these results, although the reconstruction results would suffer from inaccuracy for both CI and CSI images especially at the SNR of 30 dB, especially for Class 1, they could provide a certain level of accuracy in the case of an SNR of 40 dB. This is because the

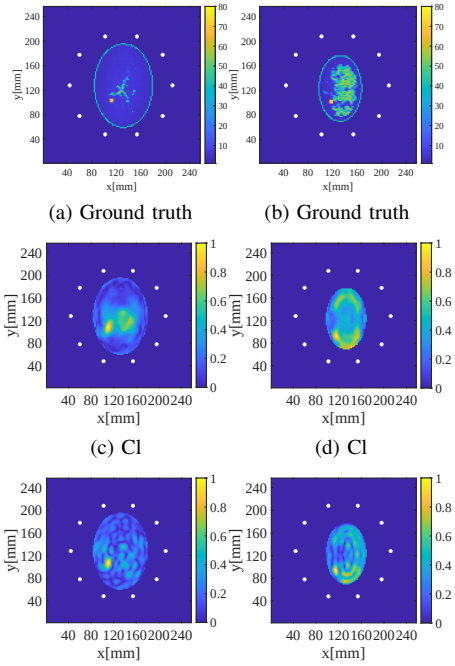

(a) Ground truth (b) Ground truth

(c) CI (d) CI

(e) Deconv. CI (f) Deconv. CI

Fig. 16: Reconstruction results for CI and CSI images at 1.27 GHz in each method at the case for off-center located cancer. 1st column: Class 1. 2nd column: Class 4.

TABLE IX: RMSE and ρ in each SNR level.

	Class	RMSE		ρ	
		$\Re[\epsilon]$	$\Im[\epsilon]$	$\Re[\epsilon]$	$\Im[\epsilon]$
SNR = ∞ dB	Class 1	5.79	2.53	0.833	0.681
	Class 4	18.34	10.22	0.409	-0.091
SNR = 40 dB	Class 1	5.08	1.73	0.873	0.855
	Class 4	15.05	9.06	0.648	0.052
SNR = 30 dB	Class 1	22.67	6.70	0.301	0.023
	Class 4	15.94	10.17	0.612	-0.008

CI or CSI images highly depend on the SNR for the inner area, which ic less than 10 dB in an SNR of 30 dB.

Furthermore, Fig. 21 and 22 also show the box plots of the RMSE for real and imaginary part of complex permittivity at Class 1 and 4, respectively, where 10 different patterns of additive noises are investigated to provide a statistically convincing conclusion. As shown in these analyses, there are non-negligible variance of RMSEs especially in the case with 30 dB SNR (4 dB SNR in considering only inner area signal), this is because a randomness of noise component affects the optimal β to generate an initial estimate. By assuming a realistic scenario, it is promising to retain a sufficient SNR (over 10 dB) for the inner area by using the matching media, such as oil, to penetrate into the inner area of the breast by suppressing the skin reflection signal.

E. Case for Multiple Frequency Extension

In the previous evaluation for the CSI based reconstruction, we assume only a single frequency at 1.27 GHz. A number of studies revealed that the multiple frequency inversion is promising for enhancing the reconstruction accuracy, especially in noisy situations, by alleviating the ill-posed conditions, or averaging effects over frequencies. Here, we introduce the simple integration scheme for muliple frequency results. At first, we obtain several complex permittivity results for each frequency. Then, these results are converted to the Debye parameter by minimizing the residual for the mean square errors, that is, the Debye fitting is applied. In this case, the two representative models as Class 1 and 4 are introduced at the absence of noise. Figures 23 and 24 show the real and imaginary parts of the complex permittivity at each frequency in Class 1, respectively, obtained by the single frequency (SF) and multiple frequency (MF) inversion

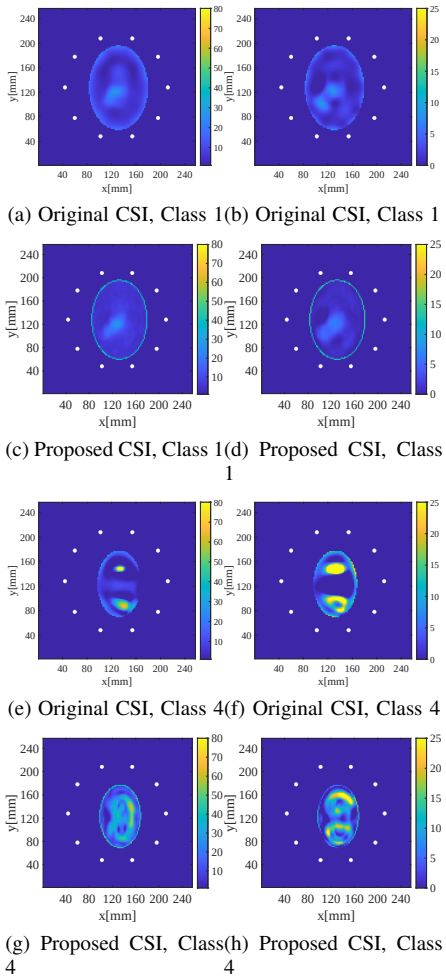

(a) Original CSI, Class 1 (b) Original CSI, Class 1

(c) Proposed CSI, Class 1 (d) Proposed CSI, Class 1

(e) Original CSI, Class 4 (f) Original CSI, Class 4

(g) Proposed CSI, Class 4 (h) Proposed CSI, Class 4

Fig. 17: Reconstruction results for CI and CSI images at 1.27 GHz in each method at the case for off-center located cancer. 1st column: $\Re[\epsilon]$. 2nd column: $\Im[\epsilon]$.

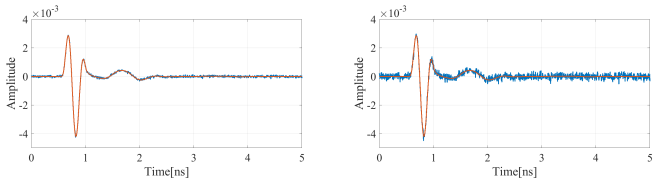

(a) SNR = 40 dB (b) SNR = 30 dB

Fig. 18: Examples of reflection responses at each SNR level. Blue denotes the response with additive noise. Red and yellow denotes the responses without and with skin reflection elimination, respectively, at the case with absence of noise.

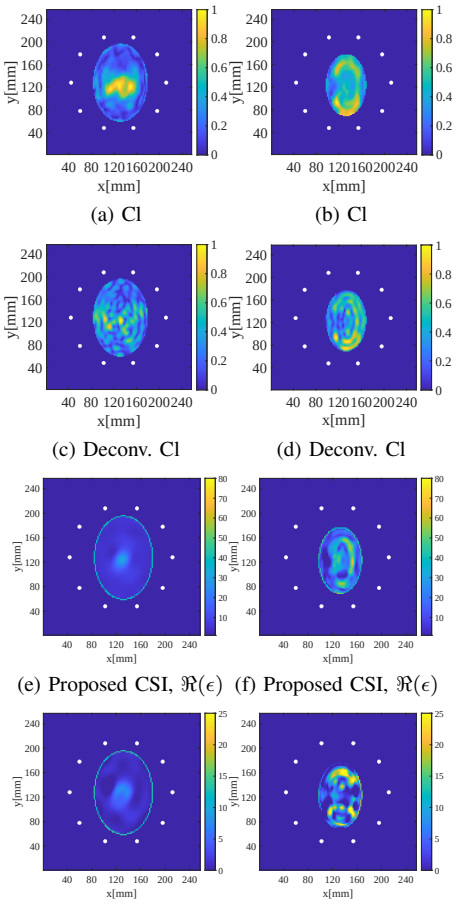

(a) CI (b) CI

(c) Deconv. CI (d) Deconv. CI

(e) Proposed CSI, $\Re(\epsilon)$ (f) Proposed CSI, $\Re(\epsilon)$

(g) Proposed CSI, $\Im(\epsilon)$ (h) Proposed CSI, $\Im(\epsilon)$

Fig. 19: Reconstruction results for CI and CSI images at 1.27 GHz in each method at the case in SNR of 40 dB. 1st column: Class 1. 2nd column: Class 4.

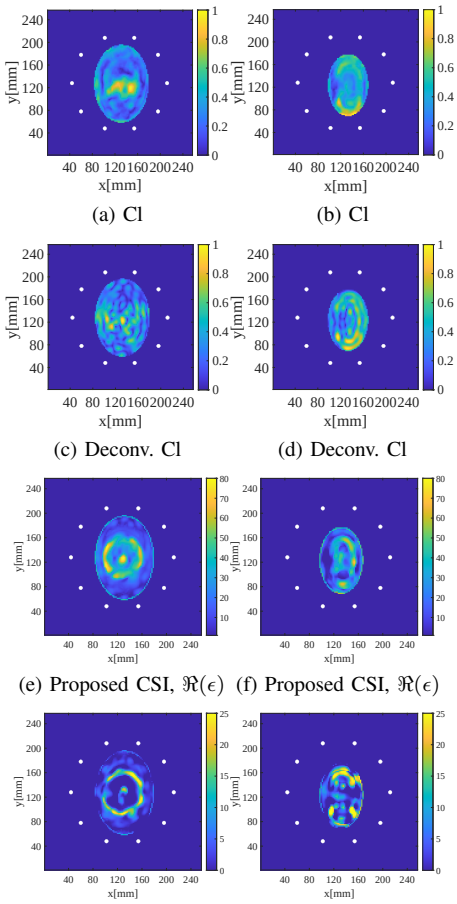

(a) CI (b) CI

(c) Deconv. CI (d) Deconv. CI

(e) Proposed CSI, $\Re(\epsilon)$ (f) Proposed CSI, $\Re(\epsilon)$

(g) Proposed CSI, $\Im(\epsilon)$ (h) Proposed CSI, $\Im(\epsilon)$

Fig. 20: Reconstruction results for CI and CSI images at 1.27 GHz in each method at the case in SNR of 30 dB. 1st column: Class 1. 2nd column: Class 4.

TABLE X: RMSE and ρ for single and multiple frequency inversion schemes in the proposed method at Condition II.

Class			RMSE		ρ	
			$\Re[\epsilon]$	$\Im[\epsilon]$	$\Re[\epsilon]$	$\Im[\epsilon]$
Class 1	1.27 GHz	SF	5.18	1.72	0.87	0.88
		MF	5.11	1.95	0.88	0.85
	2.19 GHz	SF	4.75	2.02	0.89	0.88
		MF	5.14	1.91	0.88	0.87
	3.11 GHz	SF	5.91	2.50	0.81	0.63
		MF	5.19	2.02	0.88	0.88
Class 4	1.27 GHz	SF	15.30	8.03	0.64	0.23
		MF	16.84	8.63	0.58	0.06
	2.19 GHz	SF	16.52	8.50	0.43	-0.08
		MF	16.93	6.52	0.59	0.19
	3.11 GHz	SF	20.59	6.07	0.41	0.19
		MF	17.08	5.96	0.59	0.32

schemes. Figures 25 and 26 also show the same views and conditions as those in Figures 23 and 24, but for Class 4. Table X also shows the quantitative error analysis for this case. These results demonstrated that our proposed scheme using multi-frequency data considerably enhance the reconstruction results in both real and imaginary parts of complex permittivity. This is because the variance of several single frequency results can be suppressed by the smoothing effect over multiple frequency results.

TABLE XI: Computational complexity and actual run time in each process.

Method	Step	Complexity	Run time
Original CSI		$O(N_{\rm ele}N_{\rm ROI}N_{\rm ite})$	800 s
Proposed method	1,2	$O(N_{\rm ele}N_{\rm ROI}N_{\rm FR}N_{\rm ite})$	9200 s
	3,4,5	$O(N_{\rm ele}N_{\rm ROI}N_{\rm FR})$	1500 s
	6	$O(N_{\rm ele}N_{\rm ROI}N_{\rm ite}N_{\beta})$	8000 s
	7	$O(N_{\rm ele}N_{\rm ROI}N_{\rm ite})$	800 s

F. Computational Complexity Comparison

Here, we investigate the computational complexity of each method. Table XI shows the complexity and the actual run time for each process, in using Intel Xeon Silver 4110 CPU 2.10 GHz with 384 GB RAM. Here, $N_{\rm ele}$, $N_{\rm FR}$, and $N_{\rm ROI}$ express the numbers of elements, frequency samples, and cells in the ROI, respectively, which are the same for generating the CI and CSI images. $N_{\rm ite}$ denotes the number of iterations required in the CSI. N_{β} denotes the sampling number to determine β in (18) in Sec. III-B. Here, in both the original and proposed methods, $N_{\rm ele} = 100$, $N_{\rm FR} = 58$, $N_{\rm ROI} = 2594$, $N_{\beta} = 11$, and $N_{\rm ite} = 1000$, are set. As shown

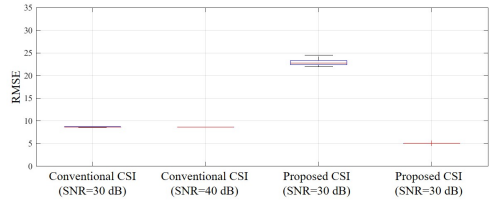

(a) RMSE for real part

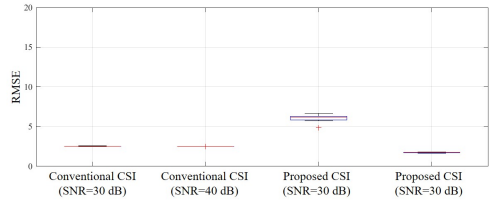

(b) RMSE for imaginary part

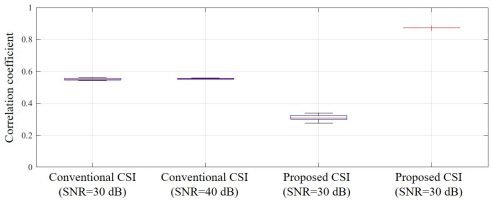

(c) ρ for real part

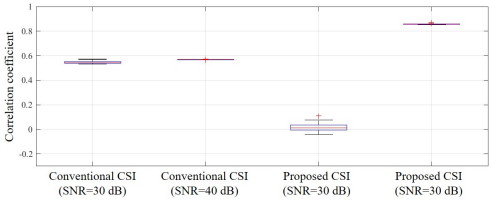

(d) ρ for imaginary part

Fig. 21: Boxplots in each SNR level and method at Class 1.

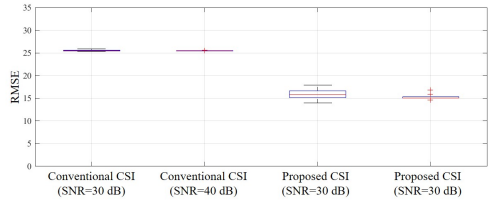

(a) RMSE for real part

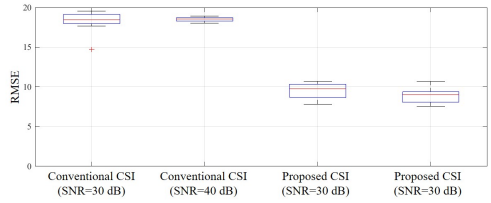

(b) RMSE for imaginary part

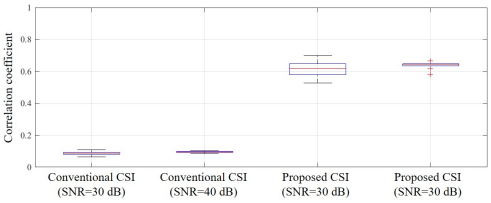

(c) ρ for real part

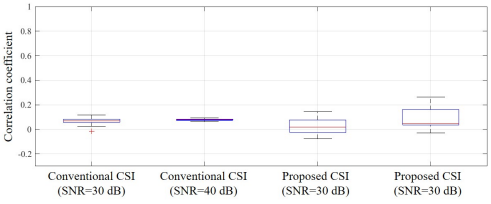

(d) ρ for imaginary part

Fig. 22: Boxplots in each SNR level and method at Class 4.

in this figure, the processes of Steps 2 and 6 require large computational times, because, in Step 2, the total fields in the ROI should be optimized at each frequency sample to obtain sufficient range resolution in the CI image, that is, an adequately wide frequency band is needed to determine the Green's function and clutter response. Meanwhile, in Step 6, the total fields in the ROI are also optimized at each β to determine an optimal initial estimate. However, the complexity of this process could be significantly reduced by the under-sampling scheme along the frequency domain. That is, if we obtain under-sampled data along the frequency band, these data can be accurately up-sampled by using the Sinc function based interpolation scheme because the sampling interval in the frequency domain (data length in the time domain) is generally sufficient to satisfy the above Nyquist criteria. The above reduction scheme should be implemented in our further study.

V. Conclusion

This paper proposes a bidirectional processing scheme between radar and tomography for the quantitative microwave imaging of breast media. The traditional CI based radar approach suffers from inaccuracy due to heterogeneity of background media, which incurs an inaccuracy for post tomography based quantitative reconstruction. Then, the CSI scheme was introduced as a tomography approach to enhance the radar-based CI image by providing an accurate form of the Green's function, assuming the heterogeneous skin-adipose media. This method also contributed a clutter suppression, particularly for the skin reflection signal, to generate these clutters using the DIE by exploiting the CSI outputs, namely the total fields in the ROI, thereby corresponding to the process of "tomography $\rightarrow$ radar". The numerical test validated that the CSI based total field optimization could provide the accurate estimate of Green's function and clutter response at the same level of FDTD based calculation. In addition, the proposed scheme introduced the CI image-enhanced CSI scheme to reproduce the quantitative reconstruction of the dielectric profile, formed as single-pole Debye parameters. The 2D Gaussian function deconvolution scheme enhanced the equivalent spatial resolution of the CI image, which was exploited for an appropriate initial estimate for the post-CSI optimization sequences. This is the process called "radar $\rightarrow$ tomography."

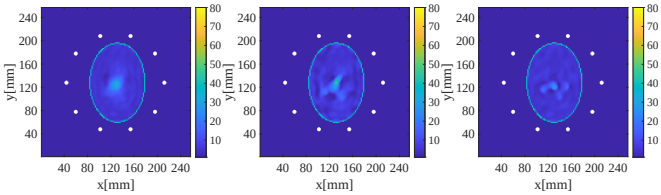

(a) SF @1.27 GHz (b) SF @2.19 GHz (c) SF @3.11 GHz

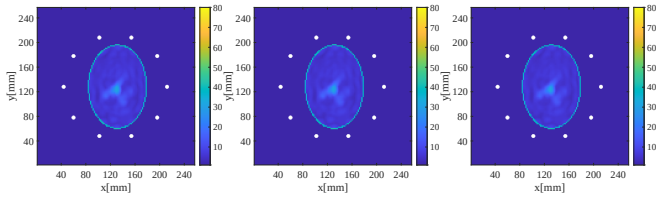

(d) MF @1.27 GHz (e) MF @2.19 GHz (f) MF @3.11 GHz

Fig. 23: Reconstruction results for real part of complex permittivity with single and multiple frequency inversion based proposed method at each frequency at Class 1.

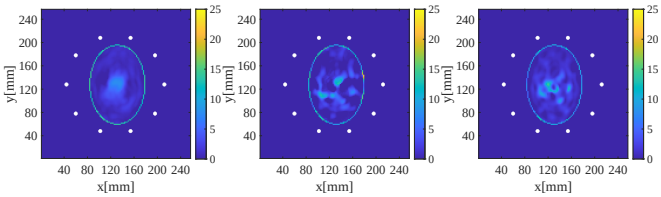

(a) SF @1.27 GHz (b) SF @2.19 GHz (c) SF @3.11 GHz

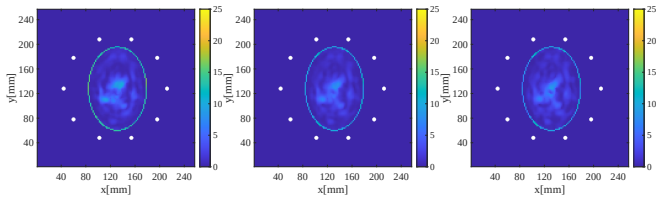

(d) MF @1.27 GHz (e) MF @2.19 GHz (f) MF @3.11 GHz

Fig. 24: Reconstruction results for imaginary part of complex permittivity with single and multiple frequency inversion based proposed method at each frequency at Class 1.

Numerical tests using the MRI-derived realistic phantom and FDTD analysis demonstrated that the proposed bidirectional processing scheme successfully improved the reconstruction accuracy of the dielectric property, even for heterogeneous and high-contrast breast media. Notably, we did not introduce any lossy-matching (coupling) media to suppress the skin reflection response, which would be promising to enhance the SNR assuming realistic cases in further investigations. Furthermore, we should note the limitation of the 2-D simulation model for realistic scenarios. In this study, we assumed a 2-D TM mode propagation, which could be modeled as a linear polarization model, such as a dipole antenna, in the 3-D model. However, some works like [33] demonstrated that the scattered field includes not only copolarized (E_z) but also cross-polarized (E_x or E_z) components, especially for highly heterogeneous media. Thus, we need the all three components of the electric total fields in the ROI, and the ill-posed condition would be extremely severe because of the considerably larger number of unknown cells.

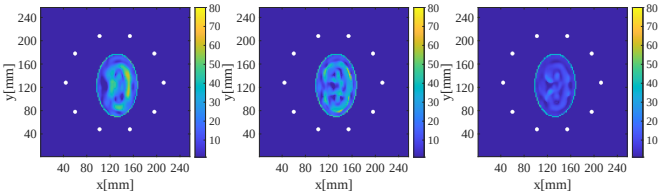

(a) SF @1.27 GHz (b) SF @2.19 GHz (c) SF @3.11 GHz

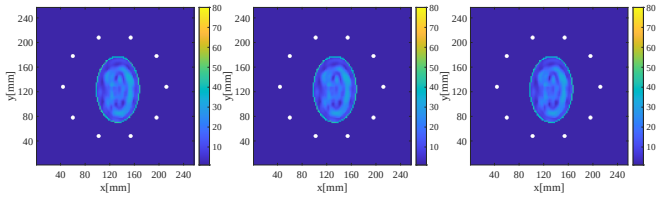

(d) MF @1.27 GHz (e) MF @2.19 GHz (f) MF @3.11 GHz

Fig. 25: Reconstruction results for real part of complex permittivity with single and multiple frequency inversion based proposed method at each frequency at Class 4.

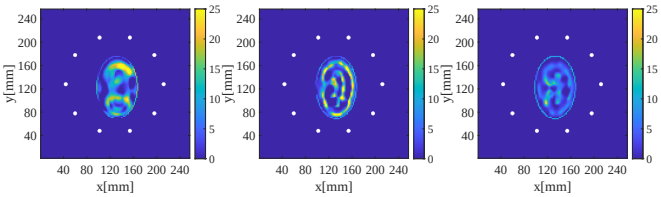

(a) SF @1.27 GHz (b) SF @2.19 GHz (c) SF @3.11 GHz

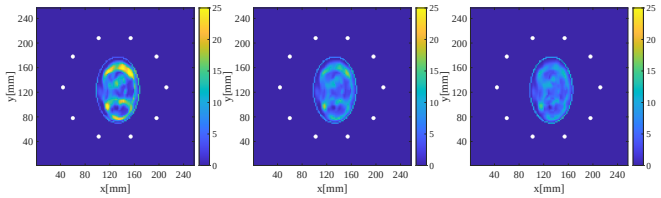

(d) MF @1.27 GHz (e) MF @2.19 GHz (f) MF @3.11 GHz

Fig. 26: Reconstruction results for imaginary part of complex permittivity with single and multiple frequency inversion based proposed method at each frequency at Class 4.

Our ongoing studies include 3D model extensions, where the under sampling or Fourier basis scheme would be introduced to drastically decrease the number of unknowns, and the experimental, or clinical investigations are included in our future scope.

REFERENCES

[1] B. M. Moloney, *et al.*, "Microwave Imaging in Breast Cancer - Results from the First-In-Human Clinical Investigation of the Wavelia System," *Academic Radiology*, Volume 29, Supplement 1, 2022, Pages S211-S222.

[2] K. Sollip, and S. Lee, "Recent Advances in Microwave Imaging for Breast Cancer Detection" *International journal of biomedical imaging*, Article ID 5054912, vol. 2016 (2016)

[3] M. Lazebnik, D. Popovic, L. McCartney, *et al.*, "A large-scale study of the ultrawideband microwave dielectric properties of normal, benign and malignant breast tissues obtained from cancer surgeries," *IOP Publishing Phys. Med. Biol.*, vol. 52, 2007, pp. 2637–2656.

[4] A. Modiri, *et al.*, "Review of breast screening: Toward clinical realization of microwave imaging", *Med. Phys.* 2017, 44, e446–e458.

[5] E. C. Fear, *et al.*, "Confocal microwave imaging for breast cancer detection: localization of tumors in three dimensions," *IEEE Transactions on Biomedical Engineering*, vol. 49, no. 8, pp. 812-822, Aug. 2002

[6] H. Song *et al.*, "Detectability of Breast Tumors in Excised Breast Tissues of Total Mastectomy by IR-UWB-Radar-Based Breast Cancer Detector," *IEEE Transactions on Biomedical Engineering*, vol. 66, no. 8, pp. 2296-2305, Aug. 2019

[7] A. Naghibi and A. R. Attari, "Near-Field Radar-Based Microwave Imaging for Breast Cancer Detection: A Study on Resolution and Image Quality," *IEEE Transactions on Antennas and Propagation*, vol. 69, no. 3, pp. 1670-1680, March 2021

[8] M. O'Halloran, *et al.*, "Improved Confocal Microwave Imaging of the breast using path-dependent signal weighting," *Proc. 2011 XXXth URSI General Assembly and Scientific Symposium*, 2011, pp. 1-4

[9] G. Umezu, Y. Yamauchi, and S. Kidera, "Contrast Source Inversion Enhanced Confocal Imaging for Highly Heterogeneous Breast Media in Microwave Mammography", *IEEE Journal of Electromagnetics, RF, and Microwaves in Medicine and Biology*, vol. 6, no. 4, pp. 494-500, Dec. 2022.

[10] P. M. van den Berg and A. Abubakar, "Contarast Source Inversion Method: State of Art," *Progress In Electromagnetics Research, PIER 34*, 2001, pp. 189–218.

[11] J. E. Johnson*, T. Takenaka and T. Tanaka, "Two-Dimensional Time-Domain Inverse Scattering for Quantitative Analysis of Breast Composition," *IEEE Transactions on Biomedical Engineering*, vol. 55, no. 8, pp. 1941-1945, Aug. 2008

[12] M. T. Bevacqua, *et al.*, "Millimeter-Waves Breast Cancer Imaging via Inverse Scattering Techniques," *IEEE Journal of Electromagnetics, RF and Microwaves in Medicine and Biology*, vol. 5, no. 3, pp. 246-253, Sept. 2021.

[13] F. Gao, B. D. Van Veen, and S. C. Hagness, "Sensitivity of the Distorted Born Iterative Method to the Initial Guess in Microwave Breast Imaging," *IEEE Trans. Antennas Propagat.*, vol. 63, no. 8, August 2015, pp. 145–154.

[14] L. M. Neira, B. D. Van Veen and S. C. Hagness, "High-Resolution Microwave Breast Imaging Using a 3-D Inverse Scattering Algorithm With a Variable-Strength Spatial Prior Constraint," *IEEE Transactions on Antennas and Propagation*, vol. 65, no. 11, pp. 6002-6014, Nov. 2017

[15] N. Abdollahi, I. Jeffrey and J. LoVetri, "Improved Tumor Detection via Quantitative Microwave Breast Imaging Using Eigenfunction-Based Prior," *IEEE Transactions on Computational Imaging*, vol. 6, pp. 1194-1202, 2020

[16] H. Sato and S. Kidera, "Noise-robust Microwave Breast Imaging Applied to Multi-frequency Contrast Source Inversion", *IEEE Journal of Electromagnetics, RF, and Microwaves in Medicine and Biology*, vol. 5, no. 2, pp. 187-193, June 2021.

[17] U. Yıldırım, *et al.*, "Continuous monitoring of hemorrhagic brain strokes via contrast source inversion," *2017 11th European Conference on Antennas and Propagation (EUCAP), 2017*, pp. 408-411

[18] V. Mariano, J. A. Tobon Vasquez, F. Vipiana "A Novel Discretization Procedure in the CSI-FEM Algorithm for Brain Stroke Microwave Imaging", *Sensors (Basel)*. 2022 Dec 20;23(1):11.

[19] M J. Burfeindt, *et al.*, "Beamforming-enhanced inverse scattering for microwave breast imaging," *IEEE Trans. Antennas Propagat.*, vol. 62, no. 10, pp. 5126-5132, Oct. 2014.

[20] A. Baran, *et al.*, "Breast Imaging Using Microwave Tomography with Radar-Based Tissue-Regions Estimation," *Progress In Electromagnetics Research*, Vol. 149, 161-171, 2014.

[21] O. Fiser et al., "UWB Bowtie Antenna for Medical Microwave Imaging Applications," *IEEE Transactions on Antennas and Propagation*, vol. 70, no. 7, pp. 5357-5372, July 2022

[22] Kurrant, D. J. and E. C. Fear, "Regional estimation of the dielectric properties of inhomogeneous objects using near-field reflection data," *Inverse Problems*, Vol. 28, No. 7, 075001, 2012.

[23] N. Abdollahi, *et al.*, "Incorporation of Ultrasonic Prior Information for Improving Quantitative Microwave Imaging of Breast," *IEEE Journal on Multiscale and Multiphysics Computational Techniques*, vol. 4, pp. 98-110, 2019

[24] N. Irishina, *et al.*, "Structural level set inversion for microwave breast screening," *Inverse Probl.*, vol. 26, 035015, 2010.

[25] T. J. Colgan, S. C. Hagness and B. D. Van Veen, "A 3-D Level Set Method for Microwave Breast Imaging," *IEEE Transactions on Biomedical Engineering*, vol. 62, no. 10, pp. 2526-2534, Oct. 2015.

[26] G. G. N. Geweid and M. A. Abdallah, "A Novel Approach for Breast Cancer Investigation and Recognition Using M-Level Set-Based Optimization Functions," *IEEE Access*, vol. 7, pp. 136343-136357, 2019.

[27] K. Noritake, S. Kidera, "Surface Clutter Suppression with FDTD Recovery Signal for Microwave UWB Mammography", *IEICE Trans. Elecron.*, vol. E103-C, No.1 Jan., 2020.

[28] W. Zhi and F. Chin, "Entropy-based time window for artifact removal in uwb imaging of breast cancer detection," *IEEE Signal Processing Letters*, Vol. 13, No. 10, 585–588, Oct., 2006.

[29] H. Song *et al*., "A Two-Stage Rotational Surface Clutter Suppression Method for Microwave Breast Imaging With Multistatic Impulse-Radar Detector," *IEEE Trans. Instrumentation and Measurement*, vol. 69, no. 12, pp. 9586-9598, Dec. 2020

[30] UWCEM, "Numerical breast phantom repository", URL: https://uwcem.ece.wisc.edu/phantomRepository.html

[31] E. Zastrow, *et al.*, "Development of Anatomically Realistic Numerical Breast Phantoms With Accurate Dielectric Properties for Modeling Microwave Interactions With the Human Breast," *IEEE Transactions on Biomedical Engineering*, vol. 55, no. 12, pp. 2792-2800, Dec. 2008.

[32] Refer:C. E. Chávez, F. Alonzo-Atienza and D. Álvarez, "Avoiding the inverse crime in the Inverse Problem of electrocardiography: estimating the shape and location of cardiac ischemia," Computing in Cardiology 2013, Zaragoza, Spain, 2013

[33] P. Zhu, H. Morimoto and S. Kidera, "Polarimetry Effect in Three-dimensional Contrast Source Inversion for Microwave Breast imaging," *Proc. 2021 IEEE USNC-URSI Radio Science Meeting (Joint with AP-S Symposium)*, Singapore, Singapore, 2021, pp. 76-77.

Mutsuki Nakajima received the B.E. degree in communication engineering and informatics from the University of Electro-Communications, Tokyo, Japan, in 2023, where she is currently pursuing the M.E. degree with the Graduate School of Informatics and Engineering. Her research interests include inverse scattering and radar signal processing for microwave bio-medical applications.

Shouhei Kidera received his B.E. degree in Electrical and Electronic Engineering from Kyoto University in 2003 and M.I. and Ph.D. degrees in Informatics from Kyoto University, Kyoto, Japan, in 2005 and 2007, respectively. In 2009, he joined as an Assistant Professor with the University of Electro-Communications, Tokyo, Japan, and he is currently a full Professor with Graduate School of Informatics and Engineering in the University of Electro-Communications, Tokyo, Japan. His current research interest is in advanced radar signal processing or electromagnetic inverse scattering issue for ultra wideband (UWB) three-dimensional sensor or bio-medical applications. He has been stayed at the Cross-Disciplinary Electromagnetics Laboratory in the University of Wisconsin Madison as the visiting researcher in 2016. He has been a Principal Investigator of the PRESTO Program of Japan Science and Technology Agency (JST) from 2017 to 2021. He was a recipient of the 2012 Ando Incentive Prize for the Study of Electronics, 2013 Young Scientist's Prize by the Japanese Minister of Education, Culture, Sports, Science and Technology (MEXT), and 2014 Funai Achievement Award, 2022 KDDI Foundation Award, Contribution Award, and 2023 RIEC Award. He is a senior member of the Institute of Electronics, Information, and Communication Engineers of Japan (IEICE), and the International Union of Radio Science (Union Radio-Scientifique Internationale, URSI), and a member of the Institute of Electrical Engineering of Japan (IEEJ), and the Japan Society of Applied Physics (JSAP).